

7620511

# PHASE UNWRAPPING AND OPTICALLY ENHANCED TILING IN DIGITAL PHOTOELASTICITY

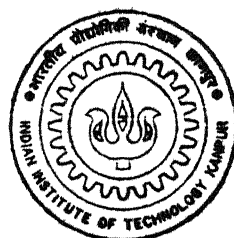
by

DANTAM SREEDHAR

TH  
ME/1998/M

ME  
1998

M  
SRE  
PHA



DEPARTMENT OF MECHANICAL ENGINEERING

**Indian Institute of Technology, Kanpur**

JUNE, 1998

# **PHASE UNWRAPPING AND OPTICALLY ENHANCED TILING IN DIGITAL PHOTOELASTICITY**

A thesis Submitted  
in partial fulfillment of the requirements  
for the degree of

**MASTER OF TECHNOLOGY**

*June, 1998*

by  
D.SREEDHAR



**DEPARTMENT OF MECHANICAL ENGINEERING  
INDIAN INSTITUTE OF TECHNOLOGY  
KANPUR - 208 016 (INDIA)**

1 JUL 1990  
**CENTRAL LIBRARY**  
I.I.T., KANPUR

MR No A 125715

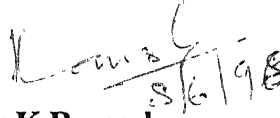
ME- 1998-M- SRE - PHA



# CERTIFICATE

This is to certify that the work contained in the thesis entitled, **PHASE UNWRAPPING AND OPTICALLY ENHANCED TILING IN DIGITAL PHOTOLEASTICITY**" by *D. Sreedhar* has been carried out under my supervision and that this work has not been submitted elsewhere for a degree.

June, 1998.



Dr.K.Ramesh

(Associate Professor)

Department of Mechanical Engineering,  
Indian Institute Of Technology, Kanpur.

## **ACKOWLEDGEMENTS**

I wish to express my deep sense of gratitude and indebtedness towards Dr. K. Ramesh for his inspiring guidance, invaluable suggestions and constructive criticism. He was always a constant source of encouragement throughout my thesis work.

I wish to thank my friends, Vishu, Malli, Ram, Siva and Siva, Rajani, Saxena and Anil, for making my stay at IIT Kanpur a memorable. I thank S. K. Mangal for his support to me for whole thesis period.

I appreciate the help provided by Mr. Radheshayam for conducting the experiments. I express my thanks to ESA laboratory staff for extending their assistance. I thank all those who contributed directly or indirectly to my thesis.

## **ABSTRACT**

*The photoelastic technique is one of the most widely used optical methods for stress analysis. Automation of photoelastic data acquisition has become essential for its wider application. The real potential of DIP hardware was realized only when the concept of identifying the fringe fields as phase maps came into existence. Phase shifting techniques in photoelasticity use the intensity data in spatial domain to extract the isochromatics over the field. This technique gives only fractional fringe order at every point in the domain. To find the total fringe order, this information is to be used in conjunction with phase unwrapping technique. A methodology for phase unwrapping is presented. For the evaluation of total fringe order by phase unwrapping, boundary detection and noise removal of the phase map are necessary. Simplified procedures to achieve these are also developed.*

*In digital fringe pattern analysis, information is usually lost in high fringe density zones due to digitization and quantization errors. The limited spatial resolution results in restricting the data acquisition in the low fringe density areas. A generic approach namely Optically Enhanced Tiling (OET) is presented to construct a composite picture from multiple optically zoomed images.*

# LIST OF CONTENTS

ABSTRACT	i
LIST OF FIGURES	ii
LIST OF TABLES	vii
CHAPTER 1 INTRODUCTION	
1.1 Introduction.....	1
1.2 Present work.....	2
1.3 Thesis Layout.....	3
CHAPTER 2 EVALUATION OF FRACTIONAL RETARDATION BY PHASE SHIFTING AND FULL FRINGE ORDER DETERMINATION BY PHASE UNWRAPPING	
2.1 Introduction.....	5
2.2 Phase Shifting In Photoelasticity .....	7
2.2.1 Patterson and Wang's Algorithm.....	8
2.2.2 Image Processing Setup .....	9
2.2.3 Experimental Evaluation And Whole Field Representation Of Fractional Retardation .....	10
2.3 Boundary Detection .....	14
2.4 Noise Removal.....	18
2.5 Algorithm For Phase Unwrapping .....	23
2.6 Representation Of Unwrapped Phase .....	25

2.6.1 Excel Plots .....	26
2.6.2 Total Fringe Order Viewing On The Image .....	27
2.7 Parameters Affecting Phase Unwrapping .....	29
2.7.1 Influence Of The Selection Of Phase Unwrapping Threshold .....	29
2.7.2 Influence Of The Location Of The Seeding Point.....	32
2.8 Use Of Tiling Procedure For Phase Unwrapping .....	33
2.8.1 Problem Of Phase Unwrapping of A Plate With A Hole.....	33
2.8.2 Ring under diametral compression .....	41
2.9 Limitations of Patterson and Wang's algorithm .....	46
2.10 Closure .....	48
 CHAPTER 3 OPTICALLY ENHANCED TILING (OET) IN DIGITAL FRINGE PATTERN ANALYSIS	
3.1 Introduction.....	49
3.2 Increase In Fringe Gradient At A Point By Digital Magnification.....	51
3.2.1 Replication .....	51
3.2.2 Linear Interpolation .....	52
3.2.3 Higher Order Interpolation .....	54
3.3 Evaluation Of Total Fringe Order of the Optically Magnified Tile.....	55
3.4 Evaluation Of The Total Fringe Order Of The OET .....	58
3.5 Cementing Of A Tile .....	63
3.5.1 Performance Of OET For The Problem Of Circular Disk Under Diametral Compression .....	65
3.6 Application Of OET To A Plate With A Hole Under Uni-axial Tension.....	69

3.6.1 Performance Of The OET For Plate With A Hole Under Uni-axial Tension.....	71
3.7 Problem of OET For Ring Under Diametral Compression .....	73
3.7.1 Performance Of The OET For Ring Under Diametral Compression .....	77
3.8 Closure .....	79
CHAPTER 4 CONCLUSIONS AND SUGGESTIONS FOR FUTURE WORK	
4.1 Conclusions.....	80
4.2 Suggestions For Future Work .....	81
APPENDIX-I	82
APPENDIX-II	83
REFERENCES	86

# LIST OF FIGURES

<b>Fig. 2.1</b> Optical arrangement for phase shifting technique.....	9
<b>Fig. 2.2</b> The sequence of six images of a circular disk under diametral compression that is recorded for phase shifting.....	11
<b>Fig. 2.3</b> Figure showing the various representation of the phase retardation.  (a) Simulated dark field (b) Simulated bright field (c) Phase map.....	12
<b>Fig. 2.4</b> Histogram of the bright field image of the circular disk under diametral compression.....	15
<b>Fig. 2.5</b> Magnified pixel representation of a curved segment on the screen.....	16
<b>Fig. 2.6</b> Boundary detection for circular disk.....	17
<b>Fig. 2.7</b> Median filtering. (a) Median filtered phase map of circular disk under diametral compression. (b) Variation of intensity along x-axis with disk center as the origin.....	18
<b>Fig. 2.8</b> 3 x 3 Masks for boundary detection. (a) 3 x 3 mask. (b) I stage of 0° scanning. (c) II stage of 0° scanning. (d) stage of 90° scanning. (e) II stage of 90° scanning. (f) I stage of 135° scanning. (g) II stage of 135° scanning. (h) I stage of 45° scanning. (i) II stage of 45° scanning.....	20
<b>Fig. 2.9</b> Present noise removal filtering. (a) Present noise filtered phase map of circular disk under diametral compression. (b) Variation of intensity along x-axis with disk center as the origin.....	22
<b>Fig. 2.10</b> Three dimensional representation of unwrapped phase for the problem of disk under diametral compression.....	27

<b>Fig. 2.11</b> Variation of intensity along vertical line passing through the load application points for the problem of circular disk under diametral compression. ....	29
<b>Fig. 2.12</b> Three dimensional representation of unwrapped phase for various phase unwrapping thresholds ( $T_p$ ). (a) $T_p = 255$ . (b) $T_p = 225$ . (c) $T_p = 180$ . (d) $T_p = 123$ . ....	31
<b>Fig. 2.13</b> Variation of total fringe order along the vertical diameter of the circular disk under diametral compression for the various phase unwrapping thresholds. ....	32
<b>Fig. 2.14</b> The sequence of six images that are recorded for phase shifting for the problem of plate with a hole. ....	34
<b>Fig. 2.15</b> Phase map for plate with a hole. (a) Phase map obtained from the phase shifting technique. (b) Modified phase map. ....	35
<b>Fig. 2.16</b> Phase map after removing the noise for the problem of plate with a hole. ....	36
<b>Fig. 2.17</b> Three dimensional representation of total fringe order for the problem of plate with a hole when primary seed point is at A of Fig. 2.16. ....	37
<b>Fig. 2.18</b> Three dimensional representation of total fringe order for the problem of plate with a hole when primary seed point is at B of Fig. 2.16. ....	37
<b>Fig. 2.19</b> Phase map showing the tiles for the problem of plate with a hole. ....	38
<b>Fig. 2.20</b> Three dimensional representation of unwrapped phase by tiling for the problem of plate with a hole. ....	39
<b>Fig. 2.21</b> Phase unwrapping by vertical tiling. (a) Phase map showing the vertical tiles for the problem of plate with a hole. (b) Three dimensional representation of unwrapped phase by tiling for the problem of plate with a hole. ....	40
<b>Fig. 2.22</b> The sequence of six images that are recorded for phase shifting for the	

problem of ring under diametral compression.....	42
<b>Fig. 2.23</b> Phase map for ring under diametral compression. (a)Phase map obtained from the phase shifting technique. (b)Modified phase map. ....	43
<b>Fig. 2.24</b> (a) Boundary detection of Phase map. (b) Phase map after removing the noise for ring under diametral compression.....	43
<b>Fig. 2.25</b> Phase map showing the tiles for ring under diametral compression.....	45
<b>Fig. 2.26</b> Three dimensional representation unwrapped phase by tiling for the problem of ring under diametral compression. ....	45
<b>Fig. 2.27</b> Isoclinics. (a) Circular disk under diametral compression. (b) Plate with a hole. (c) Ring under diametral compression. ....	47
<b>Fig. 3.1</b> Block diagram of digital magnification by replication. ....	52
<b>Fig. 3.2</b> Digital magnification of circular disk under diametral compression. (a) Original image. (b) Magnification by replication. (c) Magnification by linear interpolation. (d) Magnification by Higher order interpolation.....	53
<b>Fig. 3.3</b> Block diagram of digital magnification by linear interpolation .....	53
<b>Fig. 3.4</b> Figure showing the relationship between the overall image and the optically magnified tile. ....	55
<b>Fig. 3.5</b> The sequence of six images those are recorded for phase shifting for circular disk under diametral compression. I. Top tile. II. Bottom tile.....	56
<b>Fig. 3.6</b> Phase map. (a) Disk as a whole. (b) Top tile. (c) Bottom tile.....	57
<b>Fig. 3.7</b> Three dimensional representation of unwrapped phase for the problem of disk under diametral compression. (a) Direct evaluation. (b) Top tile. (c) Bottom tile. (d) by OET.....	59

<b>Fig. 3.8</b> Weightages of the variable mask for $m_i/m_o = 5.3$ along a row-scan .....	60
<b>Fig. 3.9</b> Figure showing the sizes of the tiles for the problem of circular disk under diametral compression .....	65
<b>Fig. 3.10</b> The theoretically reconstructed fringe pattern of disk under diametral compression .....	66
<b>Fig. 3.11</b> Comparison of fringe order variation along the $y$ -axis with disk center as the origin by various methods .....	67
<b>Fig. 3.12</b> Variation of total fringe along $y$ -axis for top magnified tile. ....	67
<b>Fig. 3.13</b> The sequence of six images those are recorded for phase shifting of magnified tile .....	68
<b>Fig. 3.14</b> Phase map. (a) One quarter of plate with a hole. (b) Magnified tile. ....	69
<b>Fig. 3.15</b> Three dimensional representation of unwrapped phase for the problem of plate with a hole. (a) Direct evaluation. (b) Magnified tile. (c) by OET.....	70
<b>Fig. 3.16</b> The theoretically reconstructed fringe pattern of disk under diametral compression for the problem of plate with a hole. ....	71
<b>Fig. 3.17</b> Comparison of fringe order variation between OET and without OET along the inner boundary of the plate with a hole.....	72
<b>Fig. 3.18</b> The sequence of six images those are recorded for phase shifting of tiles for the problem of ring under diametral compression. ....	74
<b>Fig. 3.19</b> Phase map. (a) Ring as a whole. (b) Zone1. (c) Zone2. ....	75
<b>Fig. 3.20</b> Three dimensional representation of unwrapped phase for the problem of ring under diametral compression. (a) Direct evaluation. (b) Zone1. (c) Zone2. (d) by OET.....	76

<b>Fig. 3.21</b> The theoretically reconstructed fringe pattern of ring under diametral compression .....	77
<b>Fig. 3.22</b> Comparison of fringe order variation along inner boundary of the ring by various methods.....	78
<b>Fig. A2.1</b> Distribution of stresses in a circular ring under diametral compression. ....	83

# **LIST OF TABLES**

<b>Table 2.1</b> Table showing the six optical positions required to evaluate fractional fringe order by phase shifting technique.....	8
<b>Table 2.2</b> Influence of selection of phase unwrapping threshold.....	30

## Chapter 1

# INTRODUCTION

### 1.1 Introduction

Photoelasticity deals with determination of stress fields by use of polarised light. This method is based on the temporary or artificial birefringence effect, according to which some transparent materials when subjected to a stress system behave like birefringence crystals. The birefringence in the material is retained only during the application of the loads and disappears when they are removed. Measurements of this birefringence provides data adequate for quantitative determination of the corresponding state of stress. These measurements are made with the help of an optical instrument called the polariscope, which produces optical patterns, directly related to stresses developed in the material.

A polariscope could be used to find out, namely, the maximum shear stress *i.e.*, difference in principal stresses and the orientation of principal stresses. The corresponding contours produced by the polariscope are called *isochromatic* and *isolinc fringes*. The experimentation in photoelasticity involves acquisition of these images and their interpretation. To interpret the photoelastic images, data should be collected from the images and these data should be analyzed. The main merit of photoelasticity is its simplicity in experimentation as well as in the evaluation of the stress field.

Photoelasticity still remains one of the most precise methods available for experimental stress analysis.

## 1.2 Present work

The main advantage of photoelasticity is that, it can give the stress distribution for the whole field. In conventional methods tedious compensation methods are needed to obtain the fractional fringe orders at any point other than the fringe areas. The number of data points that could be considered is also less. These procedures are quite involved and requires skill in the identification of isochromatics. Hence, automation of data acquisition and analysis to minimize these problems and to provide fast and most accurate results, has become essential.

With the advent of PC based digital image processing systems, considerable success has been achieved in automating the data acquisition from the entire field. The real potential of DIP hardware was realized only when the concept of identifying the fringe fields as phase maps came into existence. Phase shifting techniques in photoelasticity use the intensity data in spatial domain to extract the isochromatics over the field. Phase shifting interferometry will give fractional fringe order at every point in the domain. To find the total fringe order, this information is to be used in conjunction with phase unwrapping technique. A simplified procedure for phase unwrapping is discussed in this thesis.

One of the most common problems in digital fringe pattern analysis is that, information is usually lost in high fringe density zones due to digitization and quantization errors. The limited spatial resolution results in restricting the data acquisition

in the low fringe density areas. In practical engineering problems, the aim of the design engineer is to find the maximum total fringe order over the domain. However, because of the restriction of data acquisition in high fringe density zones, it is difficult to find the maximum total fringe order. The unwrapping of the phase in stress concentration zones is limited by high fringe gradient. Hence to automate the data acquisition in stress concentration zones, the fringe gradient at a point is to be reduced.

The fringe gradient at a point in the stress concentration zones can be decreased by magnifying the stress concentration zone. The image can be magnified either by digital magnification or by optical magnification. It has been observed that the intensity information required to evaluate the total fringe order is lost while digital zooming. In optical zooming, the intensity information in the high fringe density zones is retained. But few more images are needed for the analysis.

### **1.3 Thesis Layout**

In Chapter 2, the evaluation of fractional retardation by phase shifting and full fringe order determination by phase unwrapping is discussed. To limit the evaluation of total fringe order to the domain of the specimen, boundary is to be detected for the specimen. A method for boundary detection is discussed in this chapter. Presence of noise in the phase map will introduce errors in the evaluated total fringe orders. Hence, noise removal filters are necessary. Determination of full fringe order by unwrapping is demonstrated for a few example problems. To account for any arbitrary boundary and also arbitrary selection of the seed point use of tiling for phase unwrapping is implemented. The procedure is verified for a set of sample problems.

In Chapter 3, the digital magnification methods and their limitations in the evaluation of total fringe order by phase unwrapping are initially discussed. Evaluation of total fringe order by phase unwrapping using OET is then presented. The optically enhanced tiles are to be cemented on the original image to obtain the composite image. The cementing method is discussed in detail. Determination of total fringe order by using phase unwrapping technique for the composite image is demonstrated for a few example problems.

## **Chapter 2**

# **EVALUATION OF FRACTIONAL RETARDATION BY PHASE SHIFTING AND FULL FRINGE ORDER DETERMINATION BY PHASE UNWRAPPING**

### **2.1 Introduction**

The main advantage of photoelasticity is that, it can give the stress distribution for the whole field. But it gives this result as an image of fringe patterns. The main task in photoelasticity is the interpretation of these fringe patterns. In conventional methods tedious compensation methods are needed to obtain the fractional fringe orders at any point other than the fringe areas. The number of data points that could be considered is also less. These procedures are quite involved and requires skill in the identification of isochromatics. Hence, automation of data acquisition and analysis to minimize these problems and to provide fast and most accurate results, has become essential. With the advent of PC based digital image processing systems, considerable success has been achieved in automating the data acquisition from the entire field.

In the early development of digital photoelasticity, the data acquisition is limited to fringe areas. The real potential of DIP hardware was realized only when the concept of identifying the fringe fields as phase maps came into existence. This introduced new concepts in data acquisition<sup>1</sup>. It is possible to evaluate the total fringe order at every pixel in the domain and not restricted to just fringe skeletons alone.

Phase shifting techniques in photoelasticity use the intensity data in spatial domain to extract the isochromatics over the field. In these techniques, one has to record a few images corresponding to different optical arrangements for a given experimental setup. These methodologies are known as *phase shifting techniques*, in view of the specific phase shift introduced by the optical elements between the recorded images. Phase shifting interferometry will give fractional fringe order at every point in the domain. To find the total fringe order, this information is to be used in conjunction with phase unwrapping technique. Phase unwrapping procedure requires the full fringe order to be specified for at least one point in the entire domain.

To limit the evaluation of total fringe order to the domain of the specimen, boundary is to be detected for the specimen. A method for boundary detection is discussed in this chapter. Presence of noise in the phase map will introduce errors in the evaluated total fringe orders. Hence, noise removal filters are necessary. Determination of full fringe order by unwrapping is demonstrated for a few example problems. Since circular disc under diametral compression is the calibration specimen widely used in photoelasticity, the methodologies are explained with this as the specimen. The methodologies are also verified for the plate with a hole and ring under diametral compression.

## 2.2 Phase Shifting In Photoelasticity

In optical techniques such as photoelasticity used in experimental mechanics, the experimental data is recorded in the form of fringe patterns. The fringe patterns are nothing but a record of the phase difference between the light travelling in two different optical paths as intensity variations. By varying the phase difference between the beams involved, in known steps, it is possible to generate sufficient number of equations to solve for the parameters involved. The phase-shifting approach has been applied to many classical interferometric techniques. In most classical interferometers including holography, the path length of the two interfering beams are distinct and separate. In general, phase differences can be added by altering the path length of any one of the light beams. Usually the phase of the reference light beam is altered in known steps. But in photoelasticity, the two light beams cannot be treated separately but always go together. This means that a phase shift introduced in one light beam will also introduce a corresponding phase shift in the other beam also<sup>2</sup>. The change in phase, in practice, is achieved by appropriately rotating the optical elements of the polariscope.

The phase shifting concept for photoelasticity was first introduced by Hecker and Morche<sup>3</sup> in 1986. Extending the work of Hecker and Morche, Patterson and Wang<sup>4</sup> reported in 1991 a full automation procedure for photoelastic analysis. In 1992, Sarma *et al.*<sup>5</sup> reported a methodology using plane polariscope. Later in 1993, Asundi<sup>2</sup> reported a new methodology, which extended the Tardy method of compensation from a point to point approach to evaluate fractional fringe order on all points lying on the isoclinic line. In 1996, Ramesh and Ganapathy<sup>6</sup> reported a comparative study of the above methodologies and reported that among these techniques, the technique proposed by

Patterson and Wang is truly a whole field technique. Hence in the present study Patterson and Wang's algorithm is chosen to obtain the phase map.

### 2.2.1 Patterson and Wang's Algorithm

In this approach, six images are to be recorded by placing the second quarter-wave plate and the analyzer of the circular polariscope in six different settings as shown in Table 2.1. The overall optical arrangement is shown in Fig. 2.1. The fractional retardation can be calculated using the following equations.

$$\theta = \frac{1}{2} \tan^{-1} \left( \frac{i_5 - i_3}{i_4 - i_6} \right) \quad (2.1)$$

$$\delta = \tan^{-1} \left( \frac{i_5 - i_3}{(i_1 - i_2)\sin 2\theta} \right) = \tan^{-1} \left( \frac{i_4 - i_6}{(i_1 - i_2)\cos 2\theta} \right) \quad (2.2)$$

Where,  $\theta$  is the isoclinic angle and  $\delta$  is the fractional retardation or phase retardation.

S.No	II Quarter wave plate		Analyser Angle $\beta$
	$\phi$		
1	0		$\pi/4$
2	0		$3\pi/4$
3	0		0
4	$\pi/4$		$\pi/4$
5	$\pi/2$		$\pi/2$
6	$3\pi/4$		$3\pi/4$

**Table 2.1** Table showing the six optical positions required to evaluate fractional fringe order by phase shifting technique.

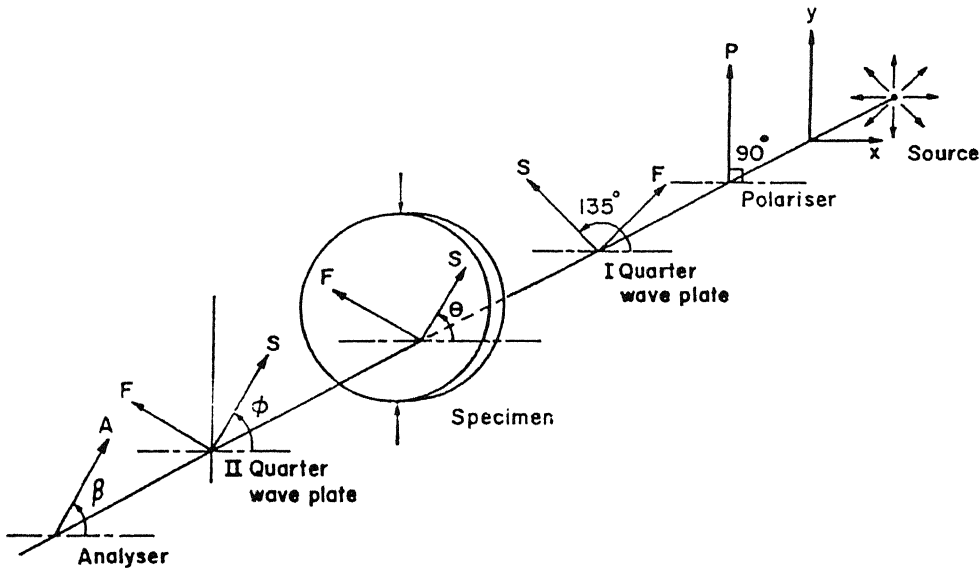


**Fig. 2.1** Optical arrangement for phase shifting technique.

### 2.2.2 Image Processing Setup

The image processing system consists of a CCD (charge coupled device) camera (TM 560 PULNIX) that has a pixel resolution of  $512 \times 512$  pixels and digitizes the images at video rates. The camera is connected to a PC based image processing system equipped with an image processing card (PIP 1024B, Matrox corporation) connected to a high

resolution video monitor. The system has in addition to PC memory, four frame buffers each of 512 x 512 pixels x 8 bits, to store the image being processed and the intermediate results.

### ***2.2.3 Experimental Evaluation And Whole Field Representation Of Fractional Retardation***

The Patterson and Wang's algorithm requires a circular polariscope. The circular polariscope has a provision to rotate each optical element independently. Sodium vapor lamp is used as monochromatic light source. An epoxy disk with a diameter of 60.14 mm, thickness of 6.28 mm and material stress fringe value ( $F_\sigma$ ) of 10.29 N/mm/fringe, which is subjected to a diametral load of 669.4 N is taken up for the analysis.

Six images are recorded by keeping the second quarter wave plate and the analyser in six different positions as shown in Table 2.1. The captured images are shown in Fig. 2.2. The Eq. (2.1) produces values of  $\theta$  which are periodic with a wave length  $\pi/2$ . It is obtained in a range from  $-\pi/4$  through zero to  $\pi/4$  which corresponds to the range of 0 to  $\pi/2$ , obtained from the classical definition of the isoclinic angle given by Frocht<sup>7</sup>. The value of the phase retardation is expressed in the range of  $-\pi$  to  $\pi$  by using atan2 function of C-program library. Dark field isochromatics can be obtained using the following equation.

$$g(x,y) = \frac{\text{abs}(\delta)}{\pi} 255.0 \quad (2.3)$$

Where  $g(x,y)$  is the grey level of the pixel at the location  $(x,y)$ . Figure 2.3(a) shows the simulated dark filed field isochromatics.

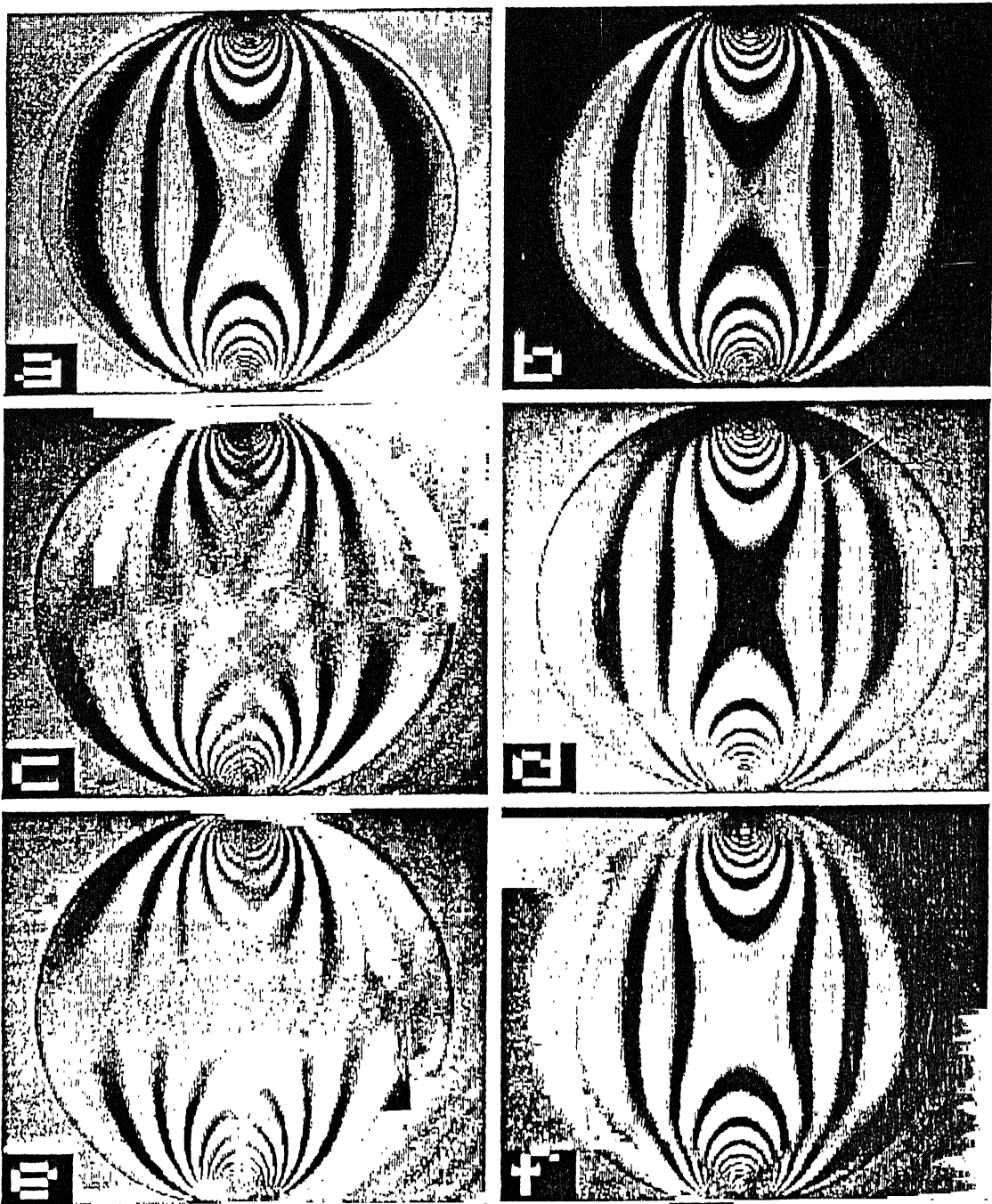
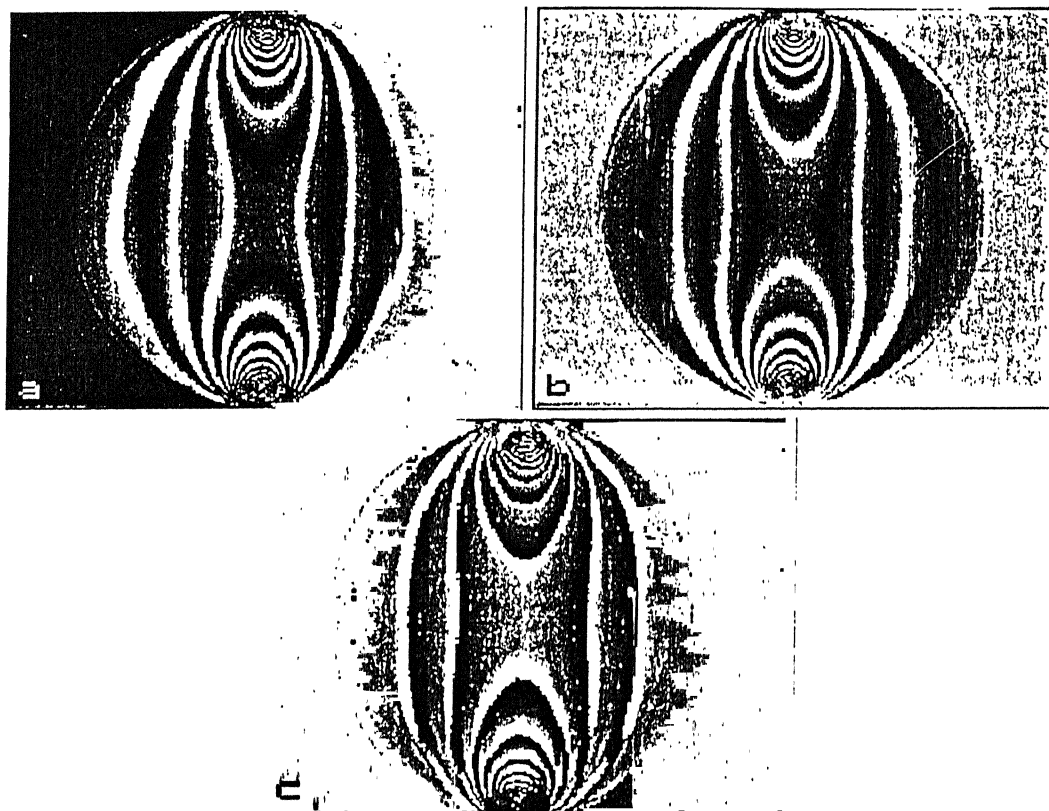


Fig. 2.2 The sequence of six images of a circular disk under diametral compression that is recorded for phase shifting.

The phase map is obtained by converting phase retardation to grey levels. The zero phase retardation corresponds to pitch black and  $2\pi$  phase retardation corresponds to pure white. So, the phase retardation is to be expressed in the range of 0 to  $2\pi$ . The phase map can be obtained from the following equations.

$$\delta = \delta + 2\pi$$

$$\delta < 0$$



**Fig. 2.3** Figure showing the various representation of the phase retardation.  
(a) Simulated dark field (b) Simulated bright field (c) Phase map.

$$g(x, y) = \frac{\delta}{2\pi} 255.0 \quad (2.4)$$

Figure 2.3(c) shows the phase map of the image. The bright field isochromatics for the image can be obtained using the following equations.

$$\delta = \delta + 2\pi \quad \delta < 0$$

$$g(x, y) = \frac{\text{abs}(\delta - \pi)}{\pi} 255.0 \quad (2.5)$$

Figure 2.3(b) shows the simulated bright field isochromatics of circular disk under diametral compression.

#### 2.2.4 Noise In The Phase Map

During the phase map calculation, when  $i_1 = i_2$  the value of phase retardation may be either  $-\pi/2$  or  $\pi/2$ . But determining whether phase retardation is positive or negative is impossible. In the present work it is assumed that the phase retardation is positive. So, when the assumption fails (*i.e.*, when  $\delta$  is  $-\pi/4$ ) the calculated phase retardation is wrong. So, these points become noise points in phase map. Similarly when  $i_4 = i_6$  and  $i_5 = i_3$ , there is indeterminacy in  $\theta$ . The value of  $\theta$  may be either  $\pi/4$  or  $-\pi/4$ . But determining whether  $\theta$  is positive or negative is impossible. In the present work it is assumed that  $\theta$  is positive and this value of  $\theta$  is used to find out fractional retardation. So, when the assumption fails (*i.e.*, when  $\theta$  is negative) the calculated phase retardation value is wrong. So, these points become noise points in the phase map.

## 2.3 Boundary Detection ✓

To limit the determination of field parameter within the region of interest (within the specimen), the image has to be segmented. The segmentation of the image will result in isolation of the region of interest from the rest of the image. Segmentation of the image is done by detecting the boundary.

In general, boundary of the image is detected using spatial filters like Roberts, Prewitt, Sobel etc.. These filters detect the edges based on abrupt change in grey levels. The edge detection algorithms not only detects the boundary, but also detects the regions in the image where there is abrupt change in grey levels. Moreover the primary interest is the detection of the boundary and not the detection of edges. The set of pixels obtained from above filters seldom characterizes a boundary completely, because of noise and breaks in boundary from non-uniform illumination. These edge detection algorithms typically are followed by other boundary detection procedures designed to assemble and link the edge pixels into meaningful boundaries. This only yield raw data in the form of pixels along a boundary. These filters are helpful to detect the edges of the images obtained in DIP applications like astronomy and defense where image recognition is the only criterion. Accuracy of the boundary is not critical. Unlike the above applications, the experimental mechanics application like photoelasticity, the shape and boundaries of the object are known. This property is used to detect the boundary accurately instead of using the above general edge detection algorithms. To make computations, the data is to be expressed as a suitable representation. In the present study this is achieved by defining two files one for row-scan and the other for column scan.

The area of the analysis can be limited by drawing the boundary around the region of interest. In the bright field arrangement of polariscope, the boundary of the image can be seen clearly [Fig. 2.2(a)]. To mark the boundary, primitives have been developed. These are line, circle, ellipse and 3-point arc. The boundary is drawn with an intensity of

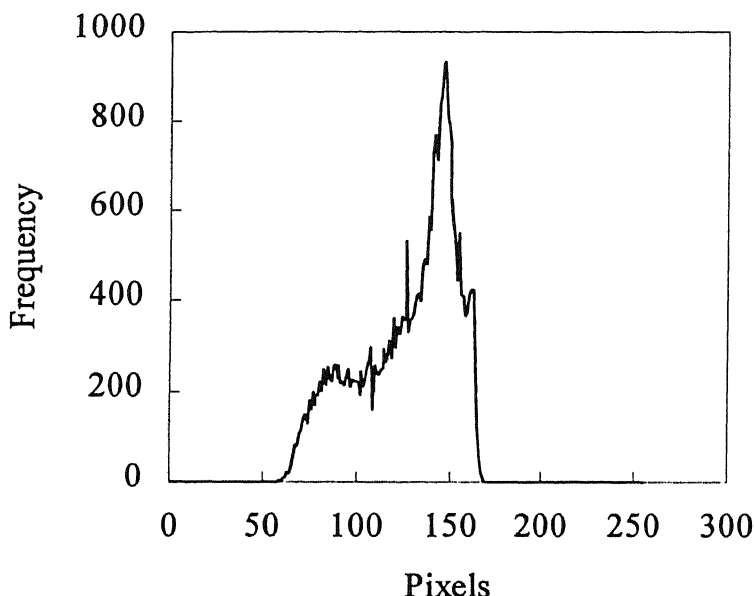


**Fig. 2.4** Histogram of the bright field image of the circular disk under diametral compression.

255. In order to quicken the boundary detection process, the algorithm accepts the actual dimensions of the specimen if available. For example to identify the circular disk boundary, one has to specify the center and the radius. Based on the optical magnification and aspect ratio of the video monitor the boundary is drawn.

Figure 2.4 shows the histogram of the bright field image of the circular disk under diametral compression. It can be observed that the maximum grey level of the image over

the entire image is 168, which is less than 255 grey level. So, any pixel with grey level value of 255 represents the boundary pixel over the entire the domain.

The image is represented as a grid of pixels and the representation of a curved boundary is shown in Fig. 2.5. In view of spatial quantization, to represent the curvature

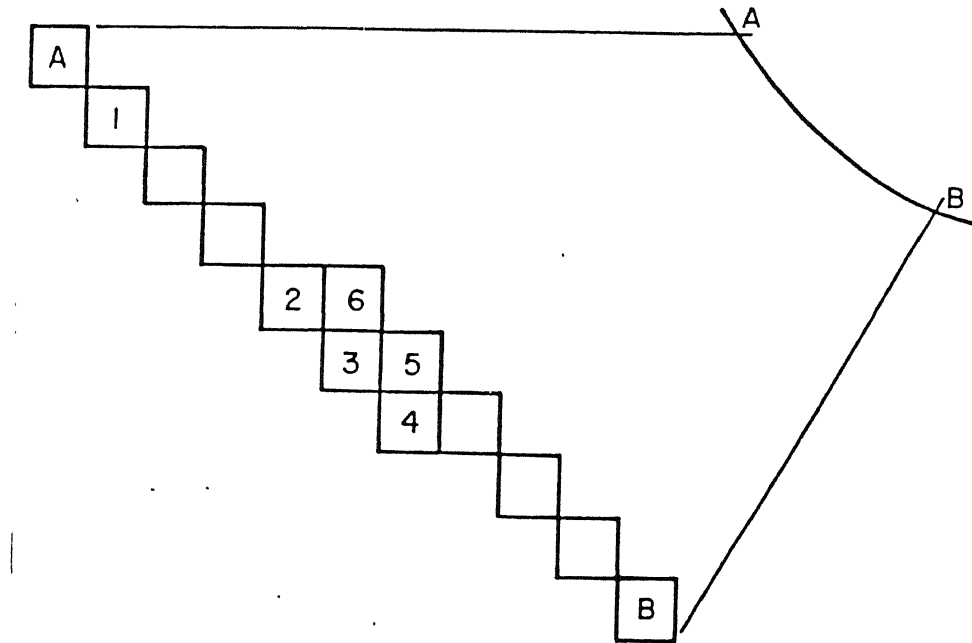


**Fig. 2.5** Magnified pixel representation of a curved segment on the screen.

more than one pixel is needed. However, for all computational purposes only the outermost pixel must be recognized as a boundary. The boundary is drawn using the primitives developed such that the outer side pixels of the circle represents the boundary of the circular disk. In the ideal case, for the curve shown in Fig. 2.5 only one pixel should represent the boundary. This is achieved by storing the positions of the pixels

which have an intensity of 255 into two separate intermediate files (scanx.dat and scany.dat), one for horizontal scanning and the other for vertical scanning. These files will have more than one pixel forming the boundary. Further processing of these files is done in which the first and last columns for every line from these files are extracted and stored into two separate files for horizontal scanning (\*.ybn) and vertical scanning (\*.xbn). In the present study the analysis of the image is limited to first quarter (256 x 256) of the quadrant. Since, the specimen will not occupy the full quarter of the quadrant, some blank lines appear in scanned files. The boundary pixels corresponding to these blank lines are 0 and 255. Hence, these blank lines are replaced with 0 and 255. The boundary detected by applying the above method on a circular disk is shown in Fig. 2.6.

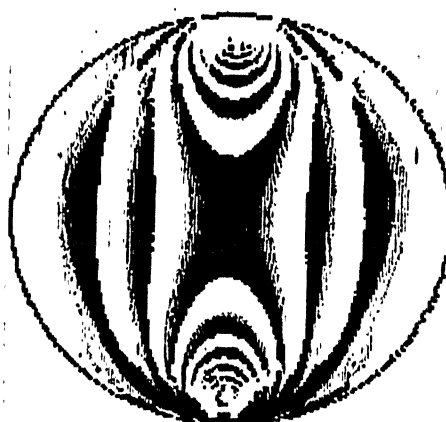
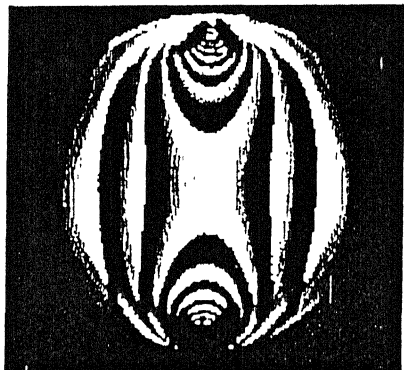


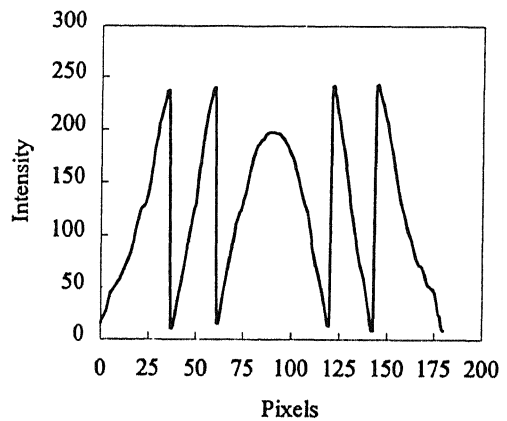
**Fig. 2.6** Boundary detection for circular disk.

## 2.4 Noise Removal

The phase map of circular disk under diametral compression has *salt and pepper noise* (binary noise) at a few points in the domain. To remove the noise from the image which has sharp edges, usually a median filter is used as other filters can destroy the sharp edges. The median filter is a nonlinear spatial filter. In median filter, the grey level of each pixel is replaced with the median of the grey levels in a neighborhood of that pixel.



(a)



(b)

**Fig. 2.7** Median filtering. (a) Median filtered phase map of circular disk under diametral compression. (b) Variation of intensity along x-axis with disk center as the origin.

Figure 2.7(a) shows the phase map after applying the median filter. Even though, the median filter preserves the sharp edges, some intensity at the sharp edges is lost. This can be seen from the intensity variation plot along the horizontal line in Fig. 2.7(b). Because

the intensity gradient at the transition of wrapped regions is the main parameter for unwrapping of the phase, any decrease in the intensity at the transition regions will affect the results in unwrapping. Thus median filter is not an ideal choice for the present application. For the removal of the noise and preserving the sharp edges, the following noise removal algorithm is used.

The noise removal algorithm will remove the binary noise based on the difference in the intensities between neighborhood pixels along the scanning direction. If the difference in intensities between the current pixel and the neighborhood pixels along the scanning direction is beyond a threshold, then the current pixel is identified as a noise pixel. Removal of noise is done by, replacing the grey level of the noise pixel with the average of grey levels of the neighborhood pixels.

Let the coefficients of the general  $3 \times 3$  mask are  $w_1, w_2, \dots, w_9$ . The mask is shown in Fig. 2.8(a). Let the grey levels of pixels under the mask corresponding to above coefficients are denoted by  $z_1, z_2, \dots, z_9$ . Let  $g(x,y)$  is the position of the pixel corresponding to the coefficient of  $w_5$ . Let the noise removal gradient threshold is  $T_n$ . The noise removal algorithm will remove the noise in two stages. Figure 2.8(b) shows the coefficients of the mask for the row scanning of the first stage. Typically the result of this stage is  $(z_5 - z_4)$ . Figure 2.8(c) shows the values of the mask coefficients for the second stage of row scanning. The result of this stage is  $(z_6 - z_5)$ . The pixel at  $g(x,y)$  is a salt noise pixel when the following condition is satisfied.

$$(z_5 - z_4) > T_n \text{ and } (z_6 - z_5) < -T_n \quad (2.6)$$

The pixel at  $g(x,y)$  is a pepper noise pixel when the following condition is satisfied.

$$(z_5 - z_4) < -T_n \text{ and } (z_6 - z_5) > T_n \quad (2.7)$$

$w_1$	$w_2$	$w_3$
$w_4$	$w_5$	$w_6$
$w_7$	$w_8$	$w_9$

(a)

0	0	0
-1	1	0
0	0	0

(b)

0	0	0
0	-1	1
0	0	0

(c)

0	-1	0
0	1	0
0	0	0

(d)

0	0	0
0	-1	0
0	1	0

(e)

-1	0	0
0	1	0
0	0	0

(f)

0	0	0
0	-1	0
0	0	1

(g)

0	0	-1
0	1	0
0	0	0

(h)

0	0	0
0	-1	0
1	0	0

(i)

**Fig. 2.8**  $3 \times 3$  Masks for boundary detection. (a)  $3 \times 3$  mask. (b) I stage of  $0^\circ$  scanning. (c) II stage of  $0^\circ$  scanning. (d) stage of  $90^\circ$  scanning. (e) II stage of  $90^\circ$  scanning. (f) I stage of  $135^\circ$  scanning. (g) II stage of  $135^\circ$  scanning. (h) I stage of  $45^\circ$  scanning. (i) II stage of  $45^\circ$  scanning.

The grey level of the noise pixel is replaced with the grey levels of the neighborhood pixels. That is  $z_5$  value is replaced with  $[(z_4 + z_6) / 2]$ .

Figures 2.8(d) and 2.8(e) are the masks for the vertical scanning of first stage and second stage respectively. The pixel at  $g(x,y)$  is a salt noise pixel when the following condition is satisfied.

$$(z_5 - z_2) > T_n \text{ and } (z_8 - z_5) < -T_n \quad (2.8)$$

The pixel at  $g(x,y)$  is a pepper noise pixel when the following condition is satisfied.

$$(z_5 - z_2) < -T_n \text{ and } (z_8 - z_5) > T_n \quad (2.9)$$

The grey level of the noise pixel is replaced with the grey levels of the neighborhood pixels. That is  $z_5$  value is replaced with  $[(z_2 + z_8) / 2]$ .

Figures 2.8(f) and 2.8(g) are the masks for  $135^\circ$  angle scanning of first stage and second stage respectively. The pixel at  $g(x,y)$  is a salt noise pixel when the following condition is satisfied.

$$(z_5 - z_1) > T_n \text{ and } (z_9 - z_5) < -T_n \quad (2.10)$$

The pixel at  $g(x,y)$  is a pepper noise pixel when the following condition is satisfied.

$$(z_5 - z_1) < -T_n \text{ and } (z_9 - z_5) > T_n \quad (2.11)$$

The grey level of the noise pixel is replaced with the grey levels of the neighborhood pixels. That is  $z_5$  value is replaced with  $[(z_1 + z_9) / 2]$ . While Fig. 2.8(h) and Fig. 2.8(i) are the mask for the  $45^\circ$  angle scanning. The pixel at  $g(x,y)$  is a salt noise pixel when the following condition is satisfied.

$$(z_5 - z_3) > T_n \text{ and } (z_7 - z_5) < -T_n \quad (2.12)$$

The pixel at  $g(x,y)$  is a pepper noise pixel when the following condition is satisfied.

$$(z_5 - z_3) < -T_n \text{ and } (z_7 - z_5) > T_n \quad (2.13)$$

The grey level of the noise pixel is replaced with the grey levels of the neighborhood pixels. That is  $z_5$  value is replaced with  $[(z_3 + z_7) / 2]$ .

The value of  $T_n$  depends on the maximum grey level gradient between neighborhood pixels in the data region and one has to select it by trial and error. In the present work a value of 123 (which corresponds to a phase of  $\pi$ ) is found to be sufficient.

Figure 2.9(a) shows the phase map of a circular disk under diametral compression after removing noise. Figure 2.9(b) shows the variation of the intensity along the horizontal diameter. It can be observed that at the transition of wrapped regions there is no loss of intensity. Thus, the phase map obtained after removing noise using the present filter is better for unwrapping than the phase map obtained after removing the noise using median

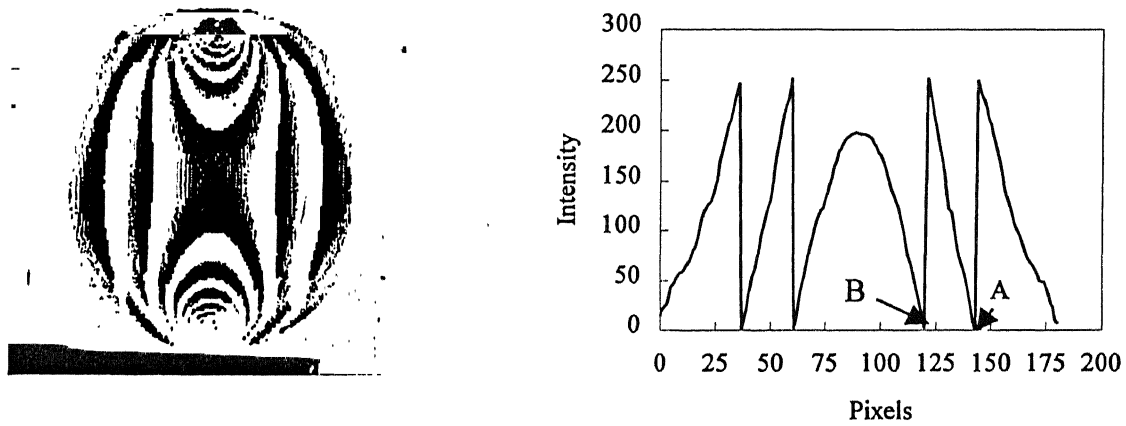


**Fig. 2.9** Present noise removal filtering. (a) Present noise filtered phase map of circular disk under diametral compression. (b) Variation of intensity along x-axis with disk center as the origin.

filter. However, when the number of noise pixels in the mask window is greater than or half the number of pixels in the mask, then both median filter and present filter fails.

## 2.5 Algorithm For Phase Unwrapping

Phase-shifting technique gives the fractional fringe order at any point in the domain. In order to find the total fringe order, phase unwrapping has to be performed. Figure 2.9(b) shows the variation of intensity in the phase map of the circular disk under diametral compression along the horizontal diameter. As the phase map represents the fractional fringe order as intensities, the plot shows the variation of the fractional fringe order along the horizontal diameter. Intensity is zero when fractional fringe order is zero and 255 when fractional fringe order is 1.0. It can be noted from the figure that the fractional fringe order increases in the direction in which the total fringe order increases, and a discontinuity in the slope occurs when the phase retardation is  $2\pi$ . If an integer fringe order is added or subtracted at the transition of wrapped regions the total fringe order can be known. The addition or subtraction can be decided by the slope of the curves. If it is positive then add otherwise subtract. The methodology however requires the total fringe order for at least at one point (primary seed point) in the domain as an input. This is to be determined by auxiliary means.

To unwrap the phase completely within the boundary, the image has to be scanned completely. A simple procedure is to scan the image column-wise. For each of these scans, one needs a seed point. This can be determined easily by initially scanning the image along a row passing through the primary seed point. The procedure can be thought of as row-wise seeding and column-wise scanning.

Let point A in Fig. 2.9(b) is the primary seed point at which the total fringe order (one) is supplied externally. It may so happen that it may not be always possible to identify the transition point exactly and in order to improve the accuracy, the software echoes back the fractional fringe order for the point selected by the user. The user then can appropriately add it with the integer part to specify the full fringe order. The variation of the intensity along the horizontal line is shown in Fig. 2.9(b). The unwrapping is first done along left direction and then along right direction. Along the left direction, the slope of the fractional fringe order between neighborhood pixels increases up to point B, hence the total fringe order increases up to point B. After point B there is a discontinuity in the slope. The discontinuity in the slope is identified by a threshold value say  $T_p$ . When the slope between neighborhood pixels is less than  $-T_p$ , the total fringe order increases by one and when the slope between the neighborhood pixels is greater than  $T_p$ , the total fringe order decreases by one. The value of  $T_p$  depends on the minimum slope between the neighborhood pixels at the transition region of wrapped phase for the whole domain. The choice of the value of  $T_p$  is discussed in the next section.

Though in principle, the fractional fringe order gradually increases in the direction of the overall fringe gradient, there can be kinks in the curve due to random noise which escaped the noise removal procedure. Since, phase unwrapping is basically a scanning procedure, this noise can easily propagate and will adversely affect the final result unless corrective measures are taken. The presence of noise or the presence of phase discontinuities is basically identified by appropriate thresholds  $T_n$  or  $T_p$  respectively. The value of  $T_p$  is usually user selectable and the performance of the phase unwrapping procedure significantly depends on this. The details are discussed later in Section 2.7.1.

Every effort must be made to select the primary seed point such that, in row-wise seeding, along the row containing the seed point no noise is present. Similarly in column wise scanning, along the column containing the seed point no noise should be present.

In some wrapped regions, the intensity neither starts with 0 nor ends with 255. The errors resulting from this behavior should be taken into consideration. The total fringe orders are calculated from the fractional fringe order between the boundary pixels ( $b_i$  and  $b_f$ ). The points within the boundary are used as seed points for the column-wise scanning. Outside the specimen boundary the total fringe order is assigned zero for computational ease. The points outside the boundary should never be used as secondary seed points for further unwrapping. Similar procedure is adopted in the column-wise seeding and row-wise scanning.

## **2.6 Representation Of Unwrapped Phase**

The total fringe orders obtained form phase unwrapping will be little useful, unless these are stored properly in files. The total fringe order is represented by its position  $(x,y)$ . The position is measured in pixels. To store the total fringe order (7 digits i.e., 2 digits integer and four digits precision in fractional part) and its location (3-digits each for x and y) of the image of size  $256 \times 256$ , the file size is approx. 1.0 MB. To reduce the handling problems of a big file, small files are created for total fringe orders. In the unwrapping of row-wise seeding and column-wise scanning, for every 15 columns of unwrapping, a new intermediate file (.N\*) is created to store the total fringe orders. For a typical  $256 \times 256$  image, 18 files are created. The number of files that can be opened in DOS is limited. So, these files are to be handled carefully.

Unwrapping for any column starts at the seed point and progress first along upward direction up to the top window coordinate and then from the seed point to the bottom window coordinate. So, the locations of the total fringe orders are not sorted. Sorting is done independently for each of the stored files. The total fringe orders from the sorted output is stored into another set of intermediate files (fri.n\*). In these files, the total fringe orders are stored in columns, *i.e.*, each column in the file corresponds to the column-wise unwrapping of total fringes orders from top to bottom. So, there are 15 columns in every file (except the last file). These files are added side by side to form the final file (\*.exl) for total fringe orders. The number of columns in the final file (\*.exl) is equal to the number of columns of the selected window of the image. The number of rows is equal to the number of rows in the selected window of the image. So, the total fringe order at any location in the file represents the total fringe order corresponding to the same location on the image when the coordinates of the location is measured from the top-left window coordinate.

### 2.6.1 Excel Plots

To plot the variation of the total fringe order over the domain, 3-D plotting softwares are necessary. The available 3-D plotting softwares in the lab are Gnuplot and Excel. Because, Gnuplot is a DOS based plotting software it is unable to handle the big data generated from unwrapping. On the other hand Excel is a windows based plotting software. It can handle big data file. Hence in the present study all the 3-D plots are drawn in Excel. The total fringe orders data file obtained from phase unwrapping can readily be used as input to Excel to plot the variation of total fringe orders over the domain. For every operation in Excel, the chart is updated. As the file size is big, even for

the Pentium processor the time taken is high of the order of 5 s. The 3-D plots become too dark and difficult to print if every line of the image is plotted. Hence, every fifth row and fifth column of total fringe orders are used from the file to plot the 3-D plots in Excel. Figure 2.10 shows the variation of total fringe order for a circular disk under diametral compression.

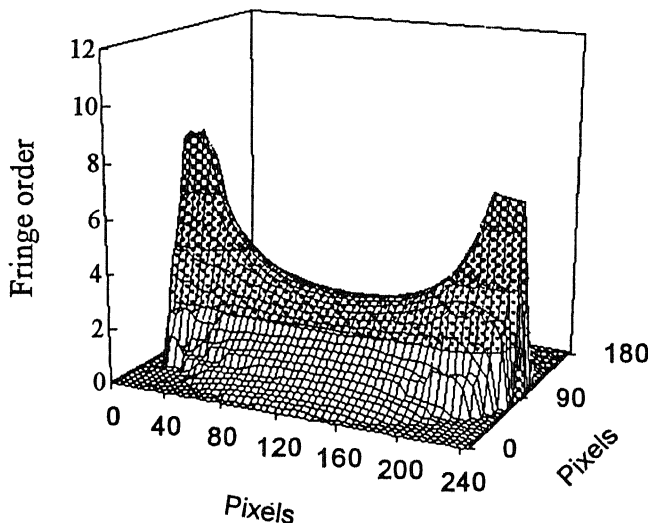


**Fig. 2.10** Three dimensional representation of unwrapped phase for the problem of disk under diametral compression.

### 2.6.2 Total Fringe Order Viewing On The Image

The stored total fringe order values are not useful, unless they are echoed on the image, corresponding to their location. Locating and reading the total fringe from file is very difficult corresponding to the input position on the image. Because the location of the new position in a file is done in terms of bytes. So, it would be rather easy if these total

fringe orders are stored in memory. For storing the total fringe orders of an image of size 256 x 256, the array size required is 0.26 MB. The memory map in C-program is discussed below.

Three areas of user memory are defined at the run time in RAM. They are the text or code area holding the .EXE file, the data area storing all the static objects, and the dynamic area (stack and heap) holding the automatic and dynamic variables. In large memory models the data areas occupy several distinct 64 KB segments. Hence the maximum size of an array that can be used as a global variable is 64 KB. Whereas the maximum size of an array that can be used as local variable is 32 KB only. The problem of allocating huge arrays is normally done by explicitly declaring the arrays as huge. However, one cannot generally pass huge data items as arguments to C library functions. The above limitations on the memory allocation can be overcome by using more than one global array to store the total fringe orders.

The total fringe order is a float number and each float number occupies 4 bytes of storage space. To occupy the 64 KB storage space, the number of total fringe orders can be read is 16000. The storage space required to store the total fringe order along one column is 0.36 KB. So, the number of columns of total fringe order that can be stored is 62. In the present study the size of each array is taken as 255 x 55. Hence to store total fringe orders of an image of size 256 x 256, the number of arrays required are 5. The total fringe order is viewed on the image by reading the total fringe order corresponding to that position from suitable array.

## 2.7 Parameters Affecting Phase Unwrapping

### 2.7.1 Influence Of The Selection Of Phase Unwrapping Threshold

A phase map is drawn in such a way that ideally when there is a discontinuity in phase, the slope should be 255. However, fringe gradient has a significant effect on the phase map. The variation of the intensity in the phase map along the vertical line passing through the load application points is shown in Fig. 2.11. It can be observed from Fig. 2.11, that at the stress concentration regions, the intensity in wrapped regions neither starts with 0 intensity nor ends with 255 intensity. This is primarily due to the fact that the fringe gradient is so high that one requires sub-pixel calculations to identify the transition zone. The lower limit of  $T_p$  is  $T_n$ . Since  $T_n$  is taken as 123, for the sake of comparison the

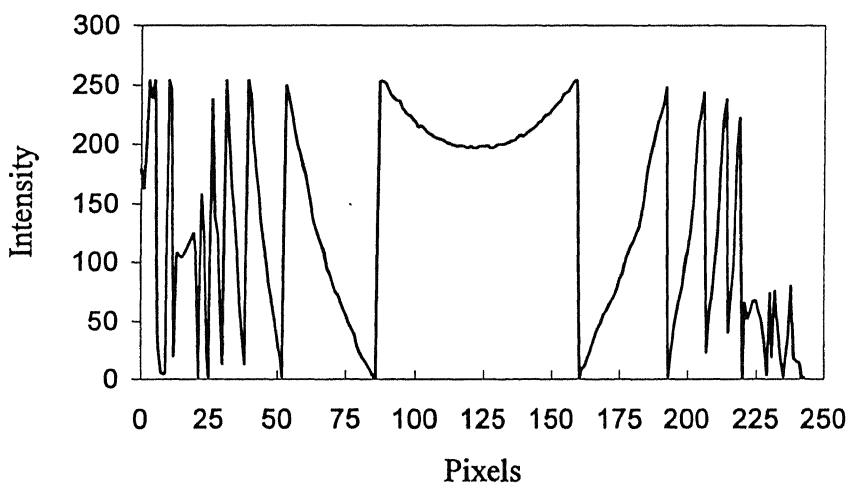


**Fig. 2.11** Variation of intensity along vertical line passing through the load application points for the problem of circular disk under diametral compression.

minimum value of  $T_p$  is selected as 123.

Figure 2.12 shows the three dimensional plots of the variation of total fringe order for the circular disk under diametral compression with phase unwrapping threshold  $T_p$  of 255, 225, 180 and 123. Figure 2.13 shows the variation of total fringe order along the vertical diameter of the circular disk under diametral compression for the above intensity slopes. The performance of the unwrapping with different thresholds values are given in Table 2.2.

Threshold ( $T_p$ )	Fringe gradient (pixels/mm)	Maximum unwrapped fringe order
225	-	2
225	0.1176	7
180	0.294	7
123	0.5176	8

**Table 2.2** Influence of selection of phase unwrapping threshold.

It can be noted from the table that, by decreasing the slope from 255 to 123, the fringe gradient that can be unwrapped is increased from 0 to 0.5176 and the evaluation of total fringe order is increased from 2 to 8. The table shows that the performance of unwrapping algorithm is maximum when the slope is 123. If the slope of the intensities between noise pixel and neighborhood pixels is more than 123, then an integer fringe order is added or

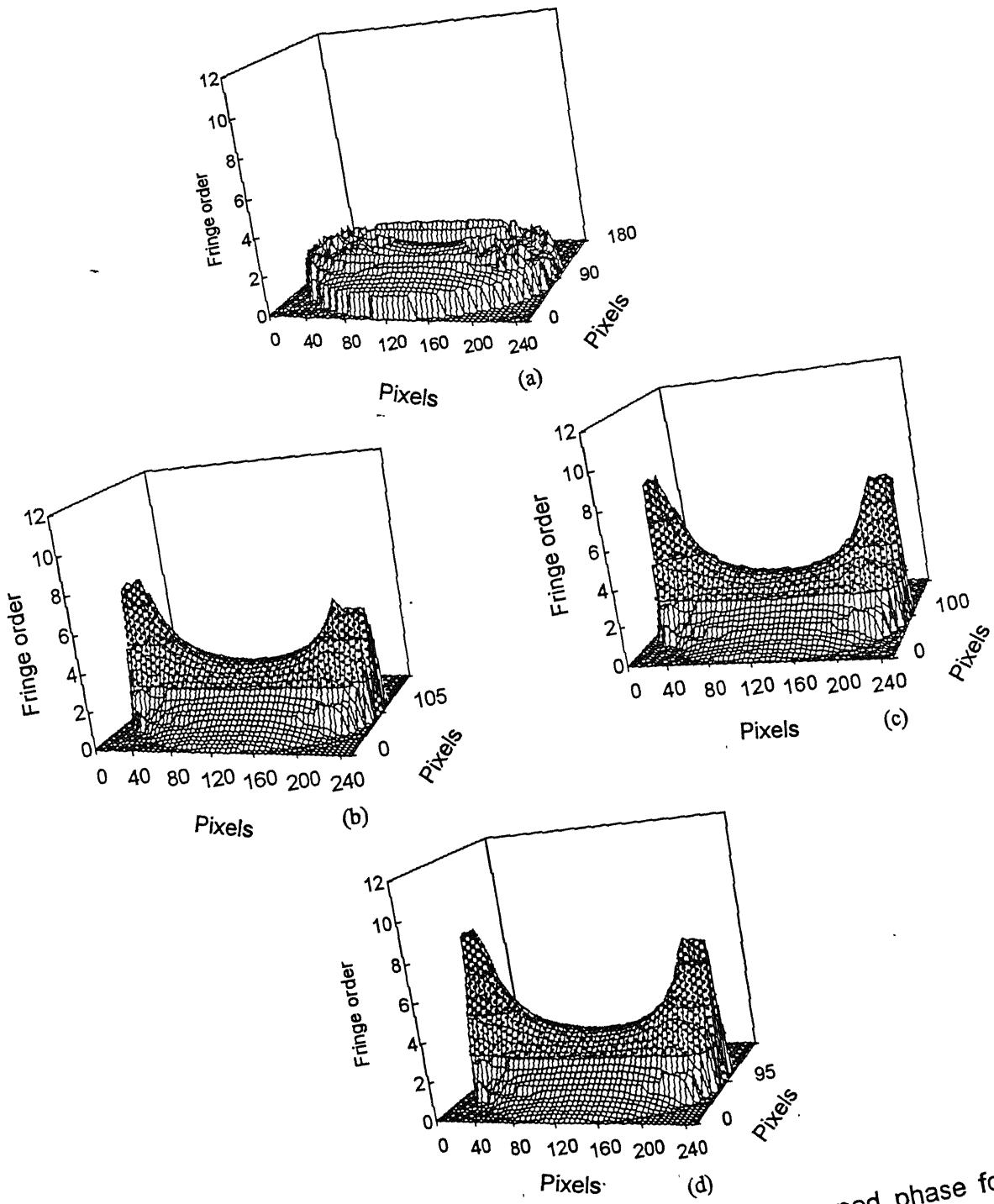


Fig. 2.12 Three dimensional representation of unwrapped phase for various phase unwrapping thresholds ( $T_p$ ).  
 (a)  $T_p = 255$ . (b)  $T_p = 225$ . (c)  $T_p = 180$ . (d)  $T_p = 123$ .

up to the boundary that is encountered along the row-wise scanning. The problem of limited unwrapping can be overcome by adopting a tiling procedure for phase unwrapping.

## **2.8 Use Of Tiling Procedure For Phase Unwrapping**

In this technique, the image is divided into tiles. Each tile will have a separate primary seed point. The primary seed points for all the tiles are linked. The total fringe orders obtained for individual tiles will be assembled together to get the total fringe order for the complete image. The tiling can be done either by dividing the image into horizontal segments or by vertical segments. In horizontal tiling, cementing of tiles is done along the horizontal direction and in vertical tiling, cementing of tiles is done along the vertical direction. Using the tiling technique, unwrapping can be done successfully for a large class of problems. The horizontal tiling for the problem of plate with a hole follows.

### **2.8.1 Problem Of Phase Unwrapping of A Plate With A Hole**

The plate with width of 37 mm, length of 174 mm and thickness of 5.26 mm is taken for analysis. The plate has a hole with inner diameter of 12.24 mm at the center of the plate. The material stress fringe value is 11.5 N/mm/fringe. A tensile load of 439.1 N is used. The specimen is made from Araldite which is prepared from CY230 resin and HY951 hardener mixed in the proportion of 100:9 by weight. Sodium vapor lamp is used as the monochromatic light source.

To take advantage of the symmetry, only one quarter of the plate with the hole is analyzed. Six images as per Table 2.1 are captured for one quarter of the plate with a hole. The images are shown in Fig. 2.14. The phase map is obtained using the procedure

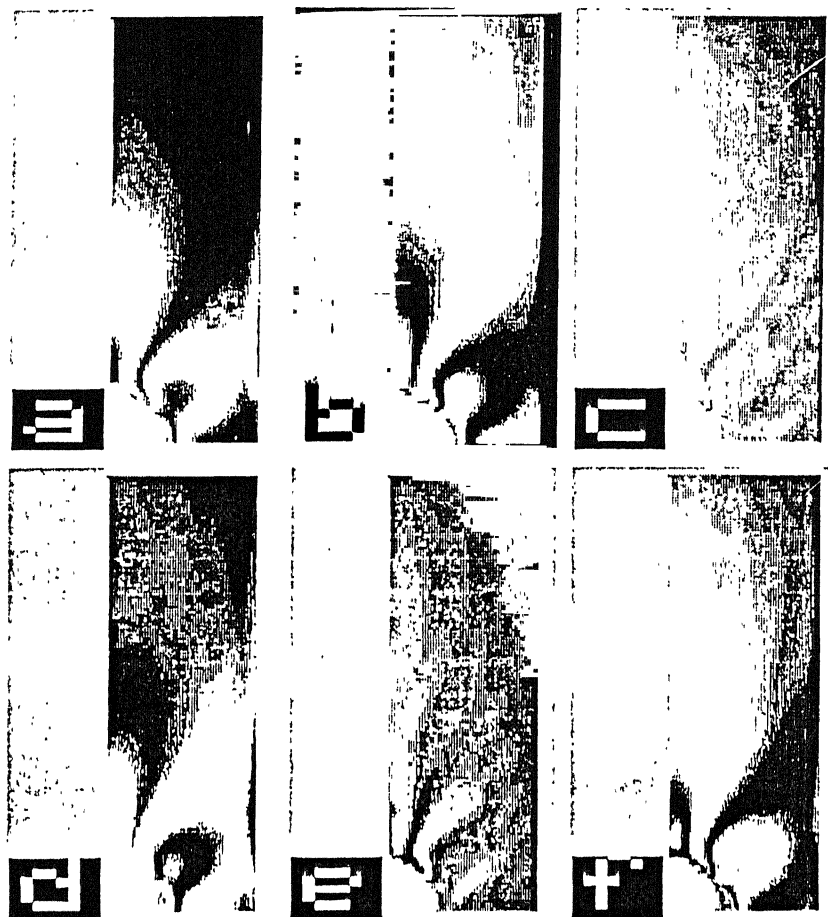


**Fig. 2.14** The sequence of six images that are recorded for phase shifting for the problem of plate with a hole.

discussed in Section 2.2 [Fig. 2.15(a)]. It can be observed from the phase map that the sign of the phase is reversed. The normal phase map can be obtained by interchanging the third image with the fifth image and fourth image with the sixth image<sup>8</sup>. Figure 2.15(b) shows the new phase map of plate with a hole after interchanging the images. Figure 2.16 show the boundary of the object and phase map after removing the noise respectively.

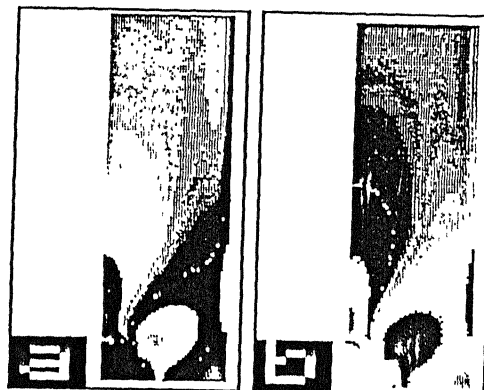


**Fig. 2.15** Phase map for plate with a hole.

- (a) Phase map obtained from the phase shifting technique.
- (b) Modified phase map.

Let us take point A (Fig. 2.16) as the primary seed point for phase unwrapping. The variation of total fringe order for the one quarter of the plate with a hole is shown in Fig. 2.17. Figure 2.18 shows the variation of the total fringe order when the primary seed point is at B (Fig. 2.16). It can be observed from Fig. 2.18, that when the primary seed

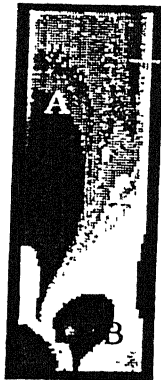


**Fig. 2.16** Phase map after removing the noise for the problem of plate with a hole.

point moves from A to B, the unwrapping algorithm is unable to unwrap the phase completely over the domain. This is because while making the secondary seed points for the column-wise scanning, the horizontal scanning crosses the boundary. It is mentioned in the previous section that the seed points outside the boundary should not be used as

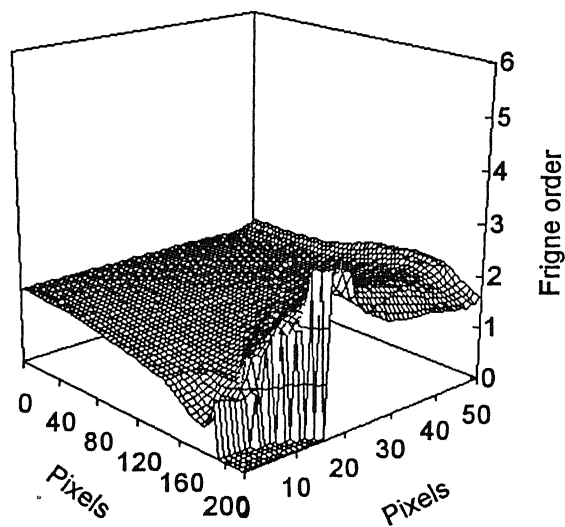


**Fig. 2.17** Three dimensional representation of total fringe order for the problem of plate with a hole when primary seed point is at A of Fig. 2.16.

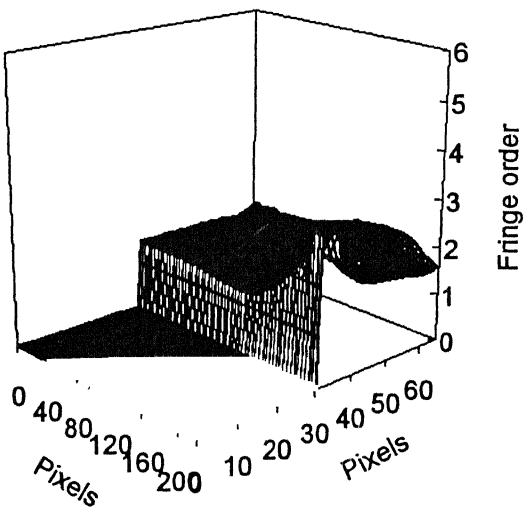


**Fig. 2.18** Three dimensional representation of total fringe order for the problem of plate with a hole when primary seed point is at B of Fig. 2.16.

secondary seed points for the column-wise scanning. Hence, the unwrapping is limited only up to the boundary that is encountered along the horizontal scanning.



**Fig. 2.19** Phase map showing the tiles for the problem of plate with a hole.

Let us take point A (Fig. 2.19) as the primary seed point for unwrapping. Let  $b_i$  and  $b_f$  are the boundary pixels along the row-wise scanning at the primary seed point. Normal unwrapping technique can unwrap the phase between the above boundary pixels. So, the size of the tile1 with input seeding at A is (number of row pixels in the window) x (number of pixels between the boundary pixels along the horizontal scan direction at A). This is shown in Fig. 2.19. Let the primary seed point for the tile2 is at B (Fig. 2.19). The

point B should be within the tile1, as total fringe order at point B will be known from unwrapped data of tile1. The size of the tile2 is (number of row pixels in the window) x

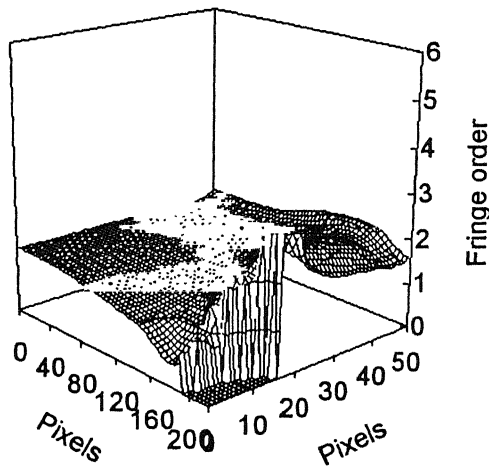


**Fig. 2.20** Three dimensional representation of unwrapped phase by tiling for the problem of plate with a hole.

(difference between the left boundary pixel along the horizontal direction and left boundary pixel of tile1). This is shown in Fig. 2.19. The total fringe order (1.48) at primary seed point of tile1 is specified. With this primary seed point, the total fringe order for the whole of tile1 is known by unwrapping. The total fringe order (2.0) at the primary seed point for tile2 is known from the unwrapped data of tile1. In this way unwrapping of all the tiles are completed. These tiles are cemented in the horizontal direction in the sequence of tile numbers (2 and 1). Figure 2.20 shows the variation of the total fringe order for one quarter of plate with a hole. It can be observed that with tiling, unwrapping can be done completely over the object for any arbitrary input of primary seed point.

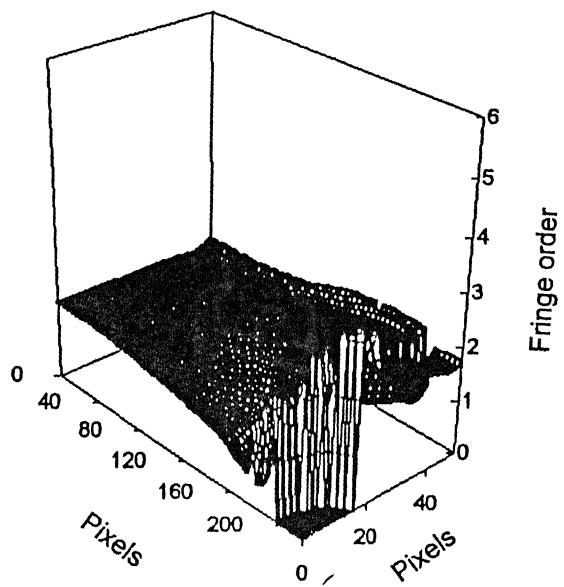
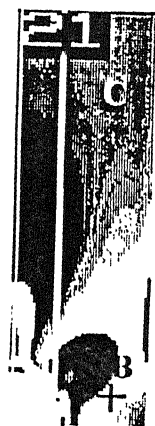


**Fig. 2.21** Phase unwrapping by vertical tiling.

(a) Phase map showing the vertical tiles for the problem of plate with a hole.

(b) Three dimensional representation of unwrapped phase by tiling for the problem of plate with a hole.

Similar to horizontal tiling, vertical tiling is also implemented. The procedure for unwrapping in vertical tiling is similar to that of the horizontal tiling. The vertical tiling and the variation of total fringe order for one quarter of plate with a hole is shown in Fig. 2.21(a) and Fig. 2.21(b) respectively.

### *2.8.2 Ring under diametral compression*

The fringe field in the case of a ring under diametral compression is much more complex than that of the circular disk under diametral compression. Already available circular ring with inner diameter of 39.76 mm, outer diameter of 80 mm, thickness of 6.26 mm and material stress fringe value of 13.5 N/mm/fringe, which is subjected to a diametral load of 523 N is taken up for analysis. Sodium vapor lamp is used as the monochromatic light source.

To take advantage of the symmetry, only one quarter of the ring is analyzed. Six images as per Table 2.1 are captured for one quarter of the ring. The images are shown in Fig. 2.22. The phase map is obtained using the procedure discussed in Section 2.2. This is shown in Fig. 2.23(a). It can be observed from the phase map that the sign of the phase is reversed after the isotropic point along horizontal diameter. The normal phase map in this region is obtained by interchanging the third image with the fifth image and fourth image with the sixth image. Figure 2.23(b) shows the new phase map of ring under diametral compression. Figure 2.24(a) and 2.24(b) show the boundary detected and the phase map after removing the noise.

It is discussed in the previous section that the unwrapping algorithm is unable to unwrap the phase completely over domain, when while making the secondary seed points the column-wise scanning, the horizontal scanning crosses the boundary. It is

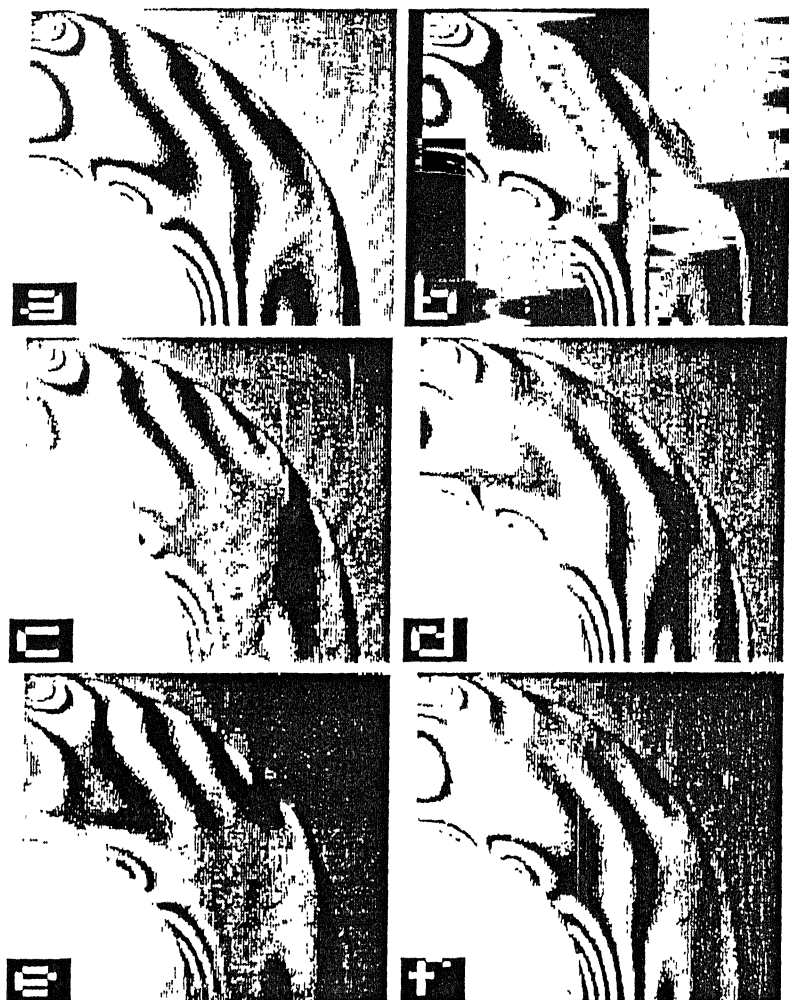


**Fig. 2.22** The sequence of six images that are recorded for phase shifting for the problem of ring under diametral compression.



**Fig. 2.23** Phase map for ring under diametral compression. (a)Phase map obtained from the phase shifting technique. (b)Modified phase map.

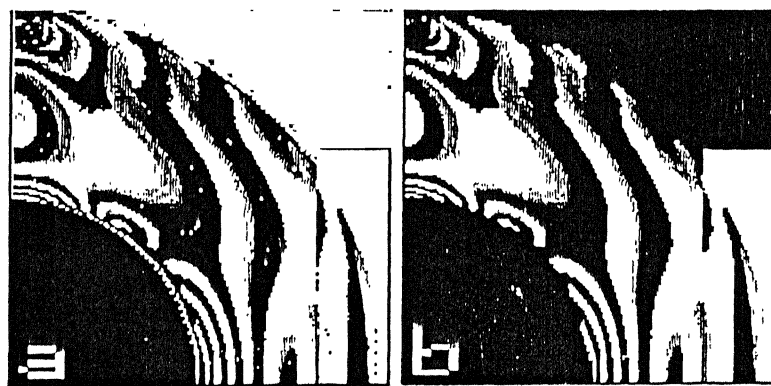


**Fig. 2.24 (a)** Boundary detection of Phase map.

**(b)** Phase map after removing the noise for ring under diametral compression.

mentioned in the Section 2.5 that the seed points outside the boundary should not be used as secondary seed points for the column-wise scanning. Hence, the unwrapping is limited only up to the boundary that is encountered along the horizontal scanning. Hence to unwrap the phase of the phase map for ring under diametral compression unwrapping by tiling procedure is adopted.

Let point A in the Fig. 2.25 is the primary seed point for the unwrapping of the phase. The tile1 is shown in Fig. 2.25. As the size of tile is not equal to the size of the domain more tilings have to be taken. Let the primary seed points for the tile2 and tile3 are B and C respectively. This is shown in Fig. 2.25. A total fringe order of 1.00 is specified at primary seed point of tile1. With this primary seed point, the total fringe order for the whole of tile1 is known by unwrapping. The total fringe order (2.4) at the primary seed point for tile2 is known from the unwrapped data of tile1. Similarly the total fringe order (0.9) at the primary seed point for tile3 is known from the unwrapped data of tile1. In this way unwrapping of all the tiles are completed. These tiles are cemented in the horizontal direction in the sequence of tile numbers (2, 1 and 3). Figure 2.26 shows the variation of the total fringe order for one quarter of ring under diametral compression.

An isochromatic fringe pattern can be looked at as a topographic representation of the field of  $\tau_{\max}$  in three dimensions. The order of fringes gives the height or level of the maximum shear stress field with respect to the plane of reference. In Fig. 2.26 certain points have been called *peaks* and *valleys* to help understand the analogy. The peaks are points where  $\tau_{\max}$  is maximum over the field. Valleys are points where  $\tau_{\max}$  is locally minimum. If the value of  $\tau_{\max}$  at a point is zero, then the point is called *isotropic* or

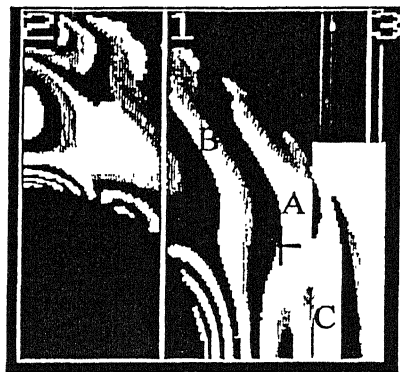


Fig. 2.25 Phase map showing the tiles for ring under diametral compression.

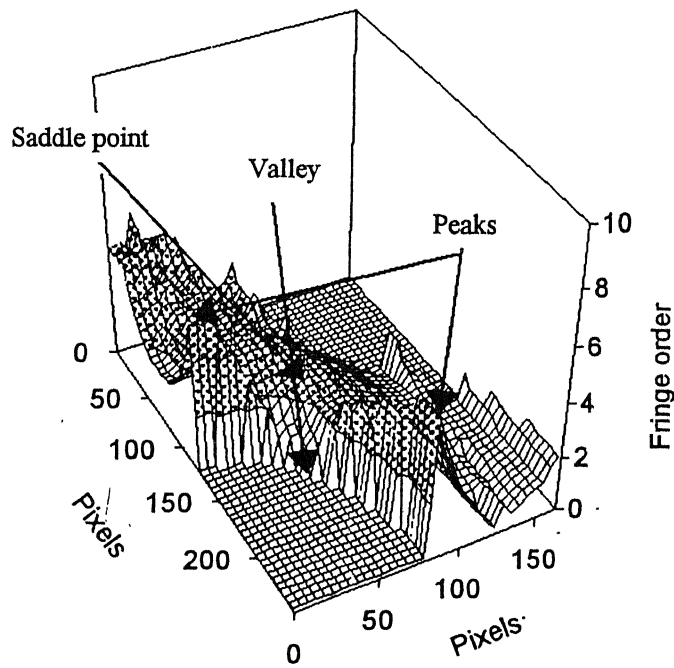


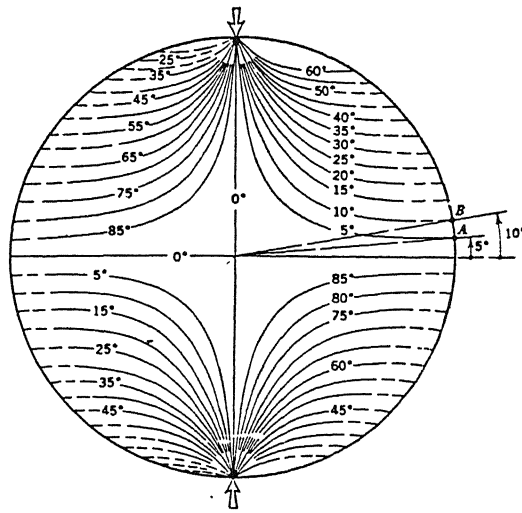
Fig. 2.26 Three dimensional representation unwrapped phase by tiling for the problem of ring under diametral compression.

*singular* point. The peak and valley points are shown in Fig. 2.26. It is to be noted that inside the field of quarter of ring , there are two valleys one is along the horizontal axis and another is along the vertical axis. If a fringe crosses itself or crosses one of the same order, then the of the fringe is called *transitional order*. If the intersection of two transition orders takes place at a point, then the point is called a *saddle point*. The transitional fringe crossing at saddle point divide the space in four regions. In two of these regions opposite to each other, the order of the fringes increases and in the other two regions the order of the fringes decreases. The saddle point for ring under diametral compression is shown in Fig. 2.26.

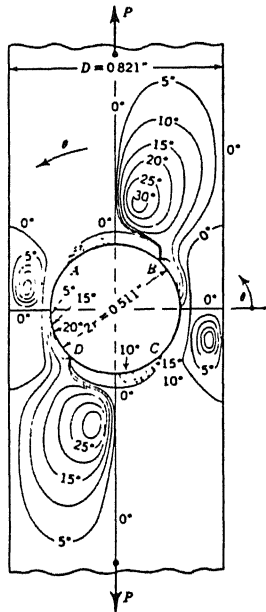
## 2.9 Limitations of Patterson and Wang's algorithm

It has been observed that in the phase maps of the plate with a hole and ring under diametral compression, the sign of the fractional retardation is changed over a region. It tells that Patterson and Wang's algorithm needs to be modified. By examining the captured images, phase map and the formulae, the following conclusions have been derived.

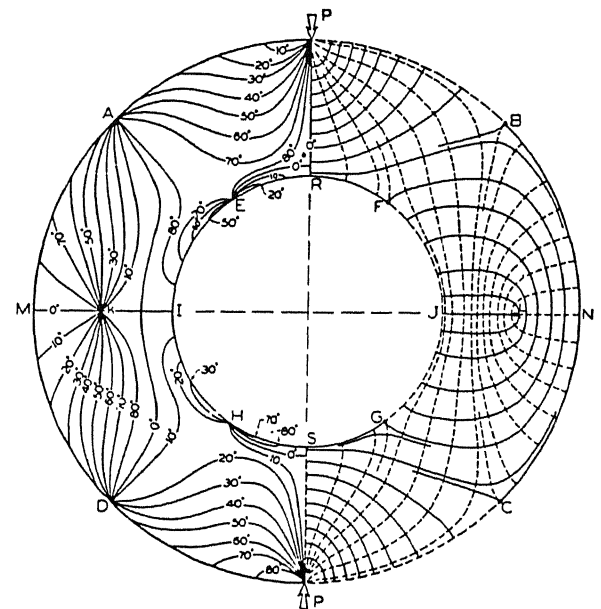
The Eq. (2.1) gives the isoclinic angle in the range of  $-\pi/4$  to  $\pi/4$  and according to the classical definition of isoclinic angle this range corresponds to 0 to  $\pi/2$  range. That is whenever the value of  $\theta$  is less than zero, an angle of  $\pi/2$  is added. There is no ambiguity exists when  $\delta$  is expressed in the range of  $-\pi$  to  $\pi$ . An ambiguity in sign of  $\delta$  exists when  $\delta$  is expressed in the range of 0 to  $2\pi$ . But in the phase map of the value of  $\delta$  is to be expressed in the range of 0 to  $2\pi$ . This results in an ambiguity of sign in some regions in the phase map. This can be limited to certain regions by considering the  $\theta$  only between



(a)



(b)



(c)

**Fig. 2.27** Isoclinics. (a) Circular disk under diametral compression. (b) Plate with a hole. (c) Ring under diametral compression.

$\pi/4$  to  $\pi/4$  instead of 0 to  $\pi/2$ . That is, the representation of phase in the phase map is valid in the range of 0 to  $\pi/4$  and above  $\pi/4$  the phase map is not valid. Figures 2.27(a), 2.27(b) and 2.27(c) show the  $\pi/4$  isoclinic angle for the problems of circular disk under diametral compression, plate with hole and ring under diametral compression respectively.

## 2.10 Closure

Evaluation of fractional retardation by phase shifting and its limitations are discussed in this chapter. Evaluation of total fringe order by phase unwrapping is also discussed. As detection of boundary and noise removal are important for the evaluation of total fringe order, algorithms to achieve these are presented. As normal unwrapping algorithm fails for certain class of problem, a technique called unwrapping by tiling is developed. The procedures are verified by estimating the total fringe order variation for a circular disk under diametral compression, plate with a hole and a ring under diametral compression.

As intensity information is lost in high fringe density areas, the extraction of more fringe orders at the stress concentration by a new technique called Optically Enhanced Tiling (OET) is discussed in the next chapter.

## **Chapter 3**

# **OPTICALLY ENHANCED TILING (OET) IN DIGITAL FRINGE PATTERN ANALYSIS**

### **3.1 Introduction**

One of the most common problems in digital fringe pattern analysis is that, information is usually lost in high fringe density zones due to digitization and quantization errors. This is mainly due to the fact that the image is identified as an assembly of pixels and for each pixel, the intensity is usually quantized to 256 grey level shades between pitch black and pure white. By increasing both spatial resolution and quantization levels, one can enhance the picture. In commonly available cameras (PAL-system) the spatial resolution is only 512 x 512. Of late, very high resolution cameras of the order 4096 x 4096 are available. However, these are quite expensive for general use. So, increasing the spatial resolution by replacing the equipment is an expensive remedy.

The limited spatial resolution results in restricting the data acquisition in the low fringe density areas. In practical engineering problems, the aim of the design engineer is to find the maximum total fringe order over the domain. The safety of the design is based on the maximum total fringe order. However, because of the restriction of data acquisition in high fringe density zones, it is difficult to find the maximum total fringe

order for practical engineering problems. Hence, improvement of data acquisition in stress concentration zones has become essential.

In the previous chapter, it has been discussed that the total fringe order over the domain can be found by unwrapping the phase of the phase map. But the unwrapping of the phase in stress concentration zones is limited by high fringe gradient. Hence to automate the data acquisition in stress concentration zones, the fringe gradient at a point is to be reduced.

The fringe gradient at a point in the stress concentration zones can be decreased by magnifying the stress concentration zone. The image can be magnified either by digital magnification or by optical magnification. In digital magnification, the region of interest is magnified by using the intensity data in the spatial domain. The digital zooming requires no additional images for the magnification. However, the intensity information required to evaluate the total fringe order is lost while zooming. In optical zooming, the intensity information in the high fringe density zones is retained. But few more images are needed for the analysis.

The digital magnification methods and their limitations in the evaluation of total fringe order by phase unwrapping are initially discussed. Evaluation of total fringe order by phase unwrapping using OET is then presented. The optically enhanced tiles are to be cemented on the original image to obtain the composite image. The cementing method is discussed in detail. Determination of total fringe order by using phase unwrapping technique for the composite image is demonstrated for a few example problems. Since circular disk under diametral compression is the mostly used calibration specimen in photoelasticity, the methodologies are explained with this as the specimen. The OET

methodology is also verified for the plate with a hole and a ring under diametral compression specimens. The phase maps obtained in the previous chapter for the above examples are used to explain the methodologies.

### 3.2 Increase In Fringe Gradient At A Point By Digital Magnification

The spatial resolution of the stress concentration zone of the image can be increased by magnifying the region of interest. The magnification of the region of interest of the image can be achieved either by digital magnification or by optical magnification. The digital magnification of region of interest is explained in this section.

The digital magnification of the region of interest can be achieved using the intensities in the spatial domain. The new grey levels required for the magnification can be obtained using the interpolation of the grey levels of the neighborhood pixels. The interpolation can be done in one of the following methods.

1. Replication
2. Linear interpolation
3. Higher order interpolation

CENTRAL LIBRARY  
I.I.T. KANPUR  
No. A 125715

#### 3.2.1 Replication

In replication, each pixel along a scan line is repeated once and each scan line is repeated. This is equivalent to taking an  $M \times N$  image and interlacing it by rows and columns of zeros to obtain a  $2M \times 2N$  matrix, and convolving the result with an array  $\mathbf{H}$ , defined as

$$\mathbf{H} = \begin{bmatrix} 1 & 1 \\ 1 & 1 \end{bmatrix} \quad (3.1)$$

The block diagram for the interpolation by replication is shown Fig. 3.1.

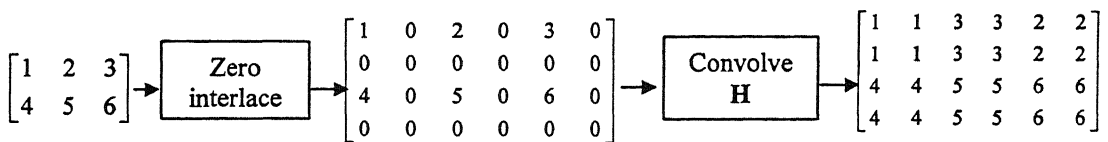
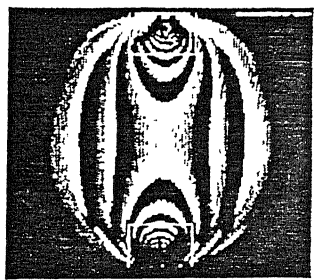


**Fig. 3.1** Block diagram of digital magnification by replication.

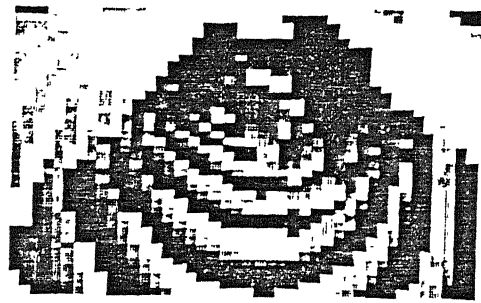
The phase map of the circular disk under diametral compression which is obtained in Section 2.2 is taken up for the analysis. This is shown in Fig. 3.2(a). The higher fringe density zones in circular disk under diametral compression are at the load application points. The high fringe density zones are shown in Fig. 3.2(a). These zones are represented as zone1 and zone2. Zone1 represents the high fringe density zone at top load application point and zone2 represents the high fringe density zone at the bottom load point. Figure 3.2(b) shows the digital zooming of the zone1 for a typical value of 5.3 times of the original zone by replication. It can be observed that the phase map obtained by the replication digital magnification hardly preserves the fractional fringe order information. Hence the magnified image obtained by replication is not suitable to evaluate the total fringe order at the high fringe density regions.

### 3.2.2 Linear Interpolation

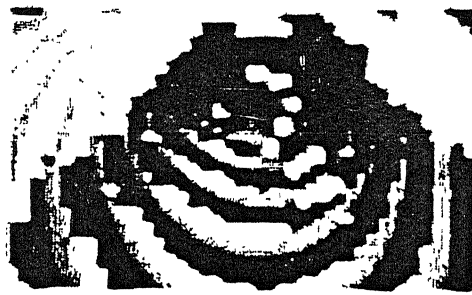
In linear interpolation, a straight line is first fitted in between pixels along a row. Then pixels along each column are interpolated along a straight line. The block diagram for the interpolation by replication is shown Fig. 3.3.



(a)



(b)



(c)



(d)

**Fig. 3.2** Digital magnification of circular disk under diametral compression. (a) Original image. (b) Magnification by replication. (c) Magnification by linear interpolation. (d) Magnification by Higher order interpolation.

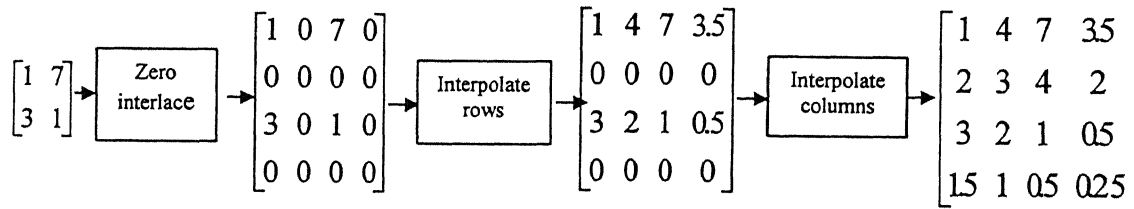


**Fig. 3.3** Block diagram of digital magnification by linear interpolation

Figure 3.2(c) shows the digital zooming of the zone1 for a typical value of 5.3 times of the original zone by linear interpolation. It can be observed that the phase map has more information than the phase map obtained by digital zooming using replication. Even though the fringe information that is retained is more, the amount of information retained by digital zooming using linear interpolation is not sufficient enough to unwrap the phase.

### **3.2.3 Higher Order Interpolation**

The fringe information of the phase map that is retained, can be increased by digital zooming of the phase map using higher order interpolation. Higher order interpolation is done by padding each row and each column of the input image  $p$  rows and  $p$  columns of zeros, respectively, and convolving it  $p$  times with  $\mathbf{H}$ . For  $p = 3$  yields a cubic spline interpolation in between the pixels.

Figure 3.2(d) shows the digital zooming of the zone1 for a typical value of 5.3 times of the original zone by cubic spline interpolation. It can be observed that the phase map has more information than the phase map obtained by digital zooming using linear interpolation. Even in digital magnification using cubic spline interpolation, the amount of fringe information retained is not sufficient enough to unwrap the phase. So, even though the digital magnification of the image increases the spatial resolution of the stress concentration zone, the amount of information retained in fringe areas is not sufficient enough to unwrap the phase by phase unwrapping. Hence, the magnification of image is to be increased by other means other than digital magnification. The evaluation of total fringe order by optical magnification is explained in next section.

### 3.3 Evaluation Of Total Fringe Order of the Optically Magnified Tile

In digital magnification no additional images are necessary to magnify the image, whereas in optical magnification requires a few more additional images to get the magnification. Initially, the overall image is captured with the maximum possible

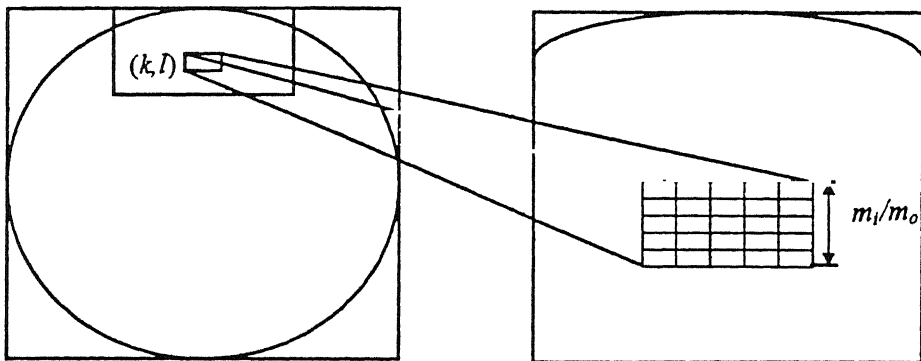


**Fig. 3.4** Figure showing the relationship between the overall image and the optically magnified tile.

magnification. Then the high fringe density zones are identified and each of these zones are separately captured with suitable higher optical magnification. Let the overall image has a magnification of  $m_o$  pixels/mm. Let the tile  $i$  has a magnification of  $m_i$  pixels/mm. For each pixel  $(k, l)$  in the original image, the magnified tile will have a block of  $m_i/m_o$  pixels. This is shown in Fig. 3.4.

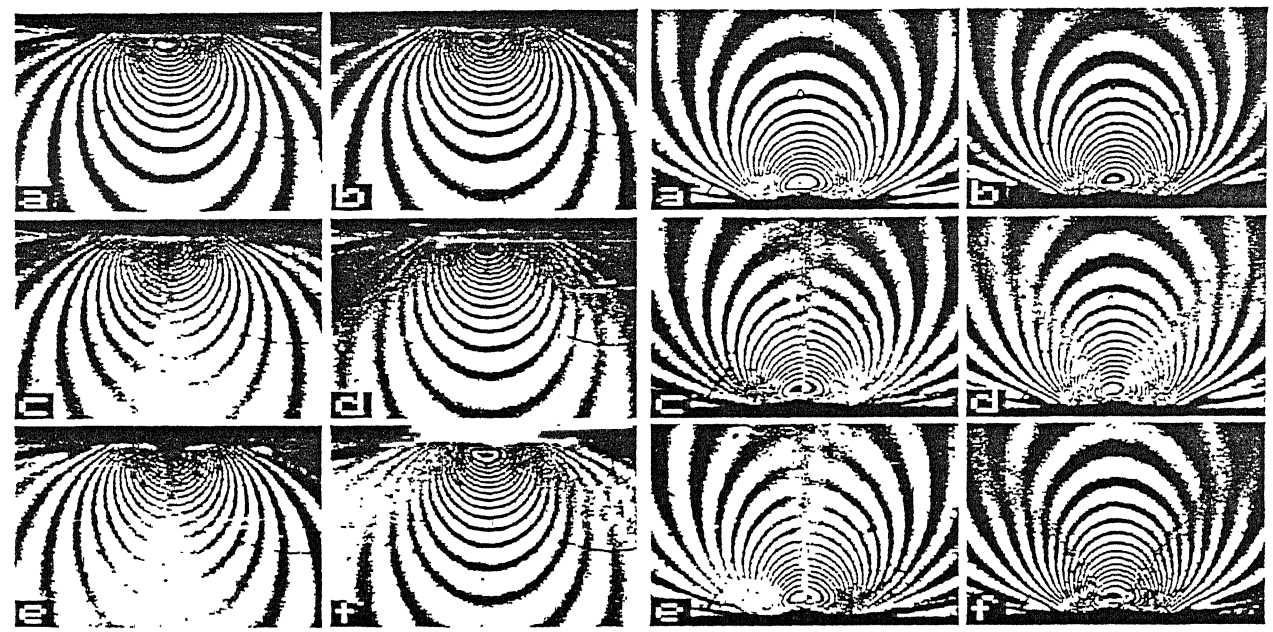


**Fig. 3.5** The sequence of six images those are recorded for phase shifting for circular disk under diametral compression. I. Top tile. II. Bottom tile.

The high fringe density zones in the circular disk under diametral compression are the load application areas. These areas are shown in Fig. 3.2(a). The magnification of the overall image is 2.97 pixels/mm *i.e.*, one mm on the original specimen is equal to 2.97 pixels on the image. Six images are captured by aligning the second quarter wave plate and analyser in the positions shown in Table 2.1, for top and bottom stress concentration zones. These images are captured with CCD camera attached with macro lens. Figures 3.5(a) and 3.5(b) show the captured images for top tile and bottom tile respectively. The phase maps for these image are obtained by the procedure discussed in Section 2.2.

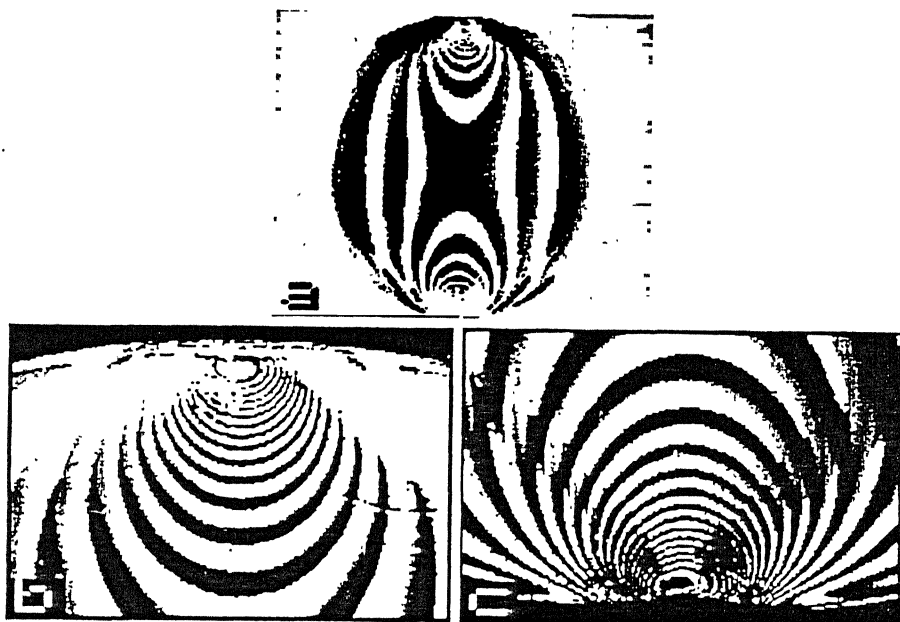


**Fig. 3.6** Phase map. (a) Disk as a whole. (b) Top tile. (c) Bottom tile.

Figures 3.6(b) and 3.6(c) show the phase maps of the top tile and bottom tile respectively. The magnification of top and bottom tiles is 16 pixels/mm. The magnification of top and bottom tiles over the original image is 5.3 *i.e.*, the ratio of  $m_i/m_o$  is equal to 5.3. Figures 3.6(b) and 3.6(c) are optically magnified images of zone1 and zone2 of the original image shown in Fig. 3.2(a). It can be observed that by optically zooming the stress concentration region, the spatial resolution is increased and at the same time the fringe information is also retained. Hence, the phase map obtained by optical magnified image is suitable to unwrap the phase by phase unwrapping and as discussed in Section 2.5 the total fringe order for these tiles are obtained. This is done for the window coordinates of (13,27) and (248,253). The procedure for the modified window coordinates is explained in Section 3.5. Figures 3.7(b) and 3.7(c) show the variation of total fringe order for top and bottom tiles respectively.

### 3.4 Evaluation Of The Total Fringe Order Of The OET

For each pixel  $(k, l)$  in the original image, the magnified tile will have a block of  $m_i/m_o$  (Fig. 3.4) pixels. The average value of the total fringe orders of these block of pixels will represent the total fringe order at  $(k, l)$  pixel in the original image. To represent the average value of the total fringe order of next block in the row-scan corresponding to  $(k, l+1)$  pixel in the original image, the blocks have to be incremented by the value of  $m_i/m_o$ . Thus, one has to find the average value of the total fringe order represented by these block of pixels and then to increment it by the value of  $(m_i/m_o)$  to achieve OET. The process is much simpler and straight forward if this ratio is integer. However, in general this expression will be a real number with an integer portion and fractional part.

The sequence of coefficients of the mask required along a row-scan are shown in Fig. 3.8 for a typical value of  $m_i/m_o$  is equal to 5.3. The important point to note is that the block of pixels involved in OET along a row scan varies from  $6 \times 6$  to  $6 \times 7$  i.e.,  $\text{Int}(m_i/m_o + 1)$  to  $\text{Int}(m_i/m_o + 2)$ . Along a column scan, it varies from  $6 \times 6$  to  $7 \times 6$ . The requirement of variable mask is achieved by taking a mask of size  $7 \times 7$ , and making the appropriate rows and columns zeros or non-zeros depending on the size of the mask. The size of the mask required to represent the total fringe order in OET is  $\text{Int}(m_i/m_o + 2) \times \text{Int}(m_i/m_o + 2)$ .

1	1	1	1	1	0.3
1	1	1	1	1	0.3
1	1	1	1	1	0.3
1	1	1	1	1	0.3
1	1	1	1	1	0.3
0.30	0.3	0.3	0.3	0.3	0.09
0.4	1	1	1	1	0.9
0.4	1	1	1	1	0.9
0.4	1	1	1	1	0.9
0.4	1	1	1	1	0.9
0.4	1	1	1	1	0.9
0.12	0.3	0.3	0.3	0.3	0.27
0.7	1	1	1	1	0.6
0.7	1	1	1	1	0.6
0.7	1	1	1	1	0.6
0.7	1	1	1	1	0.6
0.7	1	1	1	1	0.6
0.21	0.3	0.3	0.3	0.3	0.18
0.1	1	1	1	1	0.2
0.1	1	1	1	1	0.2
0.1	1	1	1	1	0.2
0.1	1	1	1	1	0.2
0.1	1	1	1	1	0.2
0.03	0.3	0.3	0.3	0.3	0.06

**Fig. 3.8** Weightages of the variable mask for  $m_i/m_o = 5.3$  along a row-scan.

Let the size of the mask is  $n \times n$ . Let the coefficients of the mask are  $w_{11}, w_{12}, \dots, w_{nn}$ . Let the row-multipliers are  $a_1, a_2, \dots, a_n$ , and column-multipliers are  $b_1, b_2, \dots, b_n$ .

.....,  $b_n$ . The coefficients of the mask are calculated using the row and column multipliers and using the following equation.

$$w_{pq} = a_p b_q \quad p = 1 \text{ to } n \text{ and } q = 1 \text{ to } n \quad (3.2)$$

At the starting point, the value of  $a_1$  and  $b_1$  are always zero and the values of  $a_2$  to  $a_{n-1}$  and  $b_2$  to  $b_{n-1}$  are 1.0, and the values of  $a_n$  and  $b_n$  are fractional part of  $m_i/m_o$ . The coefficients of the starting block are calculated using the Eq. (3.2) The total fringe order is calculated for the block of pixels as the average of the product of coefficients of the mask and their corresponding total fringe order. The total fringe orders are used only when the coefficients are non-zeros. That is, for the starting blocks, the total fringe orders are used only for coefficients of  $a_2$  to  $a_n$  and  $b_2$  to  $b_n$ .

The row-multipliers for the other blocks in the row-scan are calculated using the following equations.

$$a_1 = 1 - a_n \quad (3.3)$$

$$a_p = 1.0 \quad p = 2 \text{ to } n-2 \quad (3.4)$$

$$a_{n-1} = \begin{cases} \frac{m_i}{m_o} - \sum_{p=1}^{n-2} a_p & \text{when } a_{n-1} < 1.0 \\ 1.0 & \text{when } a_{n-1} > 1.0 \end{cases} \quad (3.5)$$

$$a_n = \frac{m_i}{m_o} - \sum_{p=1}^{n-1} a_p \quad (3.6)$$

If  $a_n = 0$ , then all the subscripts is incremented by one i.e.,  $a_1$  becomes  $a_2$ ,  $a_2$  becomes  $a_3$  and so on. Therefore, in that case  $a_1$  becomes zero. The total fringe order along the row-scan calculated for every block of pixels as the average of the product of

coefficients and their corresponding total fringe order. The total fringe orders are used only when the coefficients are non-zero.

Column-multipliers are calculated for the other blocks of vertical scan using the following equations.

$$b_1 = 1 - b_n \quad (3.7)$$

$$b_p = 1.0 \quad p = 2 \text{ to } n-2 \quad (3.8)$$

$$b_{n-1} = \begin{cases} \frac{m_i}{m_o} - \sum_{p=1}^{n-2} b_p & \text{when } b_{n-1} < 1.0 \\ 1.0 & \text{when } b_{n-1} > 1.0 \end{cases} \quad (3.9)$$

$$b_n = \frac{m_i}{m_o} - \sum_{p=1}^{n-1} b_p \quad (3.10)$$

If  $b_n = 0$ , then all the subscripts is incremented by one. Therefore, in that case  $b_1 = 0$ . The total fringe order along the column-scan calculated for every block of pixels as the average of the product of coefficients and their corresponding total fringe order. The total fringe orders are used only when the coefficients are non-zero. Using the above row-multipliers and column-multipliers the total fringe order for every block of pixels is calculated over the domain in the magnified tile.

For the problem of circular disk with a hole, the value of  $m_i/m_o$  is 5.3, i.e., each pixel in zone1 of the original image, the magnified tile will have a block of 5.3 pixels. The total fringe orders correspond to every block of pixel in the magnified tile is calculated using the above procedure. The number of blocks of pixels along the horizontal

direction is 44. The number of blocks of pixels along the vertical direction is 42. So, the size of zone1 in the original image is  $44 \times 42$ .

### 3.5 Cementing Of A Tile

The total fringe order at each pixel in high fringe density zones of the original image is replaced by the one appropriately obtained from the optically magnified tile. To cement the tile in the original image the position of at least one of the block of the pixels in the magnified image is to be known with respect to the original image.

Ideally, the calculation of the experimental parameter (total fringe order) should start at the specified block in the magnified tile and should continue to calculate the total fringe order for the whole domain. To make easier computations, the calculation of total fringe order starts at the top left window coordinates, and the total fringe order is calculated first along the horizontal direction and then along the vertical direction. To minimize errors, the position of the top left window is to be located exactly with respect to the specified point (origin) of the magnified tile. As it is impossible to locate the block of pixels, the center of the block is taken as the origin. But the size of the block is a real number with an integer portion and a fractional part. As it is impossible to specify the fractional number as pixels, the fractional number is converted into the nearest integer. The top left coordinate of the window is realigned such that the distance between this coordinate and the top left coordinate of origin block will have minimum error in multiples of  $m_i/m_o$ . Similarly, the bottom right coordinate of the window is realigned.

The load application point on the original image and on the magnified tile (optically enhanced top tile) are taken as the reference points for cementing of circular

disk under diametral compression. The point with coordinates (136, 29) is chosen as origin for top tile. Because  $m_i/m_o$  is 5.3, the size of the origin block is 5 x 5, with origin as center. Let the window coordinates (10, 27) and (250, 253) are taken to unwrap the phase of the top tile. The coordinates of the origin block are (134, 27) and (138, 31). The distance between the  $x$ -coordinate of top left window coordinates and the  $x$ -coordinate of top left coordinates of origin block is 125. This is not multiples of 5.3. When 125 is divided by 5.3, the remainder is 3.1. So, the realigned  $x$ -coordinate of top left window is 13. Similarly the realigned  $y$ -coordinate of top left window is 27. Similar procedure is adopted to find out the right bottom window coordinate. The realigned right bottom window coordinates are (248, 253).

The window coordinates of the zone1 on the original image is obtained using the window coordinates of the magnified tile and the reference points. The distance of top left window coordinate of zone1 from the reference point of the original image is obtained as the ratio of the distance from the top left window coordinate of magnified tile to its origin and  $m_i/m_o$ . The size of the zone1 is known from the procedure discussed in the previous section. The bottom right coordinate of the window is obtained by adding the size of the zone1 to the top left window coordinate. Similar procedure is adopted to get the window coordinates for zone2.

Let the reference point for top tile in disk under diametral compression is at window coordinates (134, 9). So, the top left window coordinates is (111, 9), and the bottom right window coordinates is (155, 52). Figure 3.9 shows the sizes of the top and bottom tiles on the original image. The total fringe orders within the zones are replaced

by the one appropriately obtained from the optically magnified tile. Figure 3.7(d) shows the variation of the total fringe order for circular disk under diametral compression.

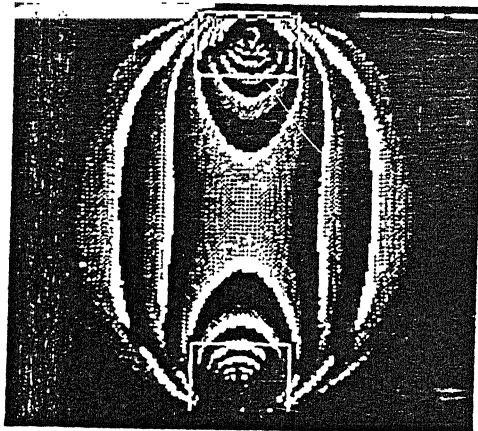


**Fig. 3.9** Figure showing the sizes of the tiles for the problem of circular disk under diametral compression.

### *3.5.1 Performance Of OET For The Problem Of Circular Disk Under Diametral Compression*

To calculate the theoretical fringe orders at a point on the disk under diametral compression, the material stress fringe value  $F_\sigma$  is to be known. The  $F_\sigma$  of the circular disk under diametral compression is calculated using the least squares method for 85 data points collected from the fringe areas. The  $F_\sigma$  value is found to be 10.29 N/mm/fringe.

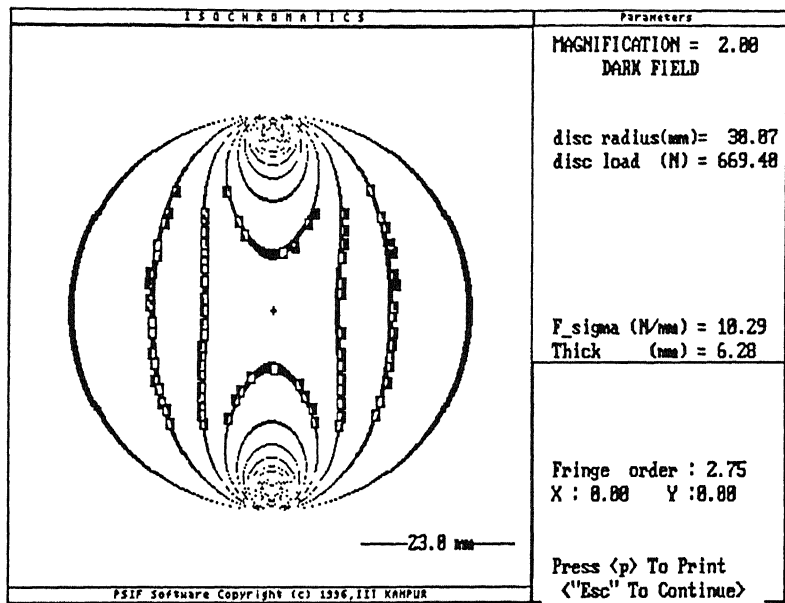
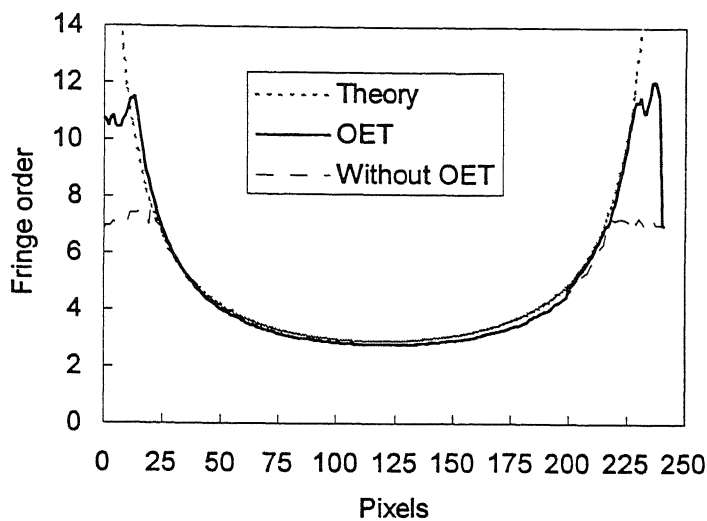


**Fig. 3.10** The theoretically reconstructed fringe pattern of disk under diametral compression.

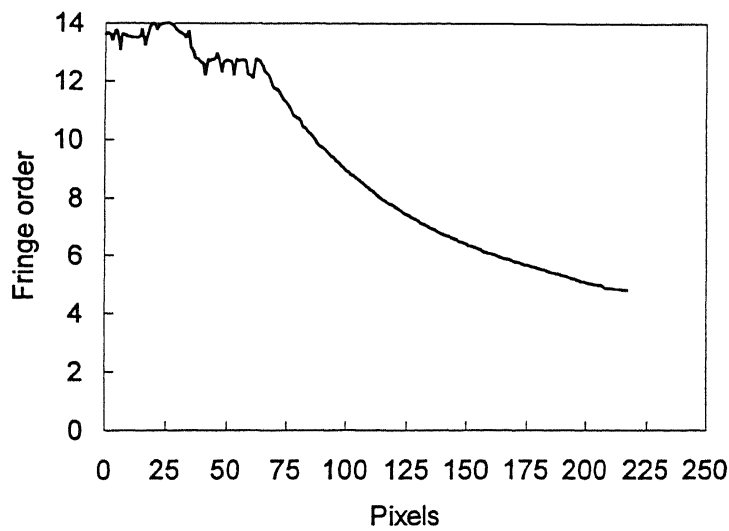
The accuracy of this value is verified by reconstructing the fringe pattern and comparing it with the original fringe pattern. The reconstructed fringe pattern is shown in Fig. 3.10.

Figure 3.11 compares the variation of total fringe order along the vertical line passing through the load application points with theory (Appendix-I). From the figure it is clear that by direct evaluation, the total fringe order is limited to a value of 7 with a corresponding fringe gradient of 0.294 fringe/pixel. With OET, the fringe order

resolvable is up to 11 and fringe gradient is increased to 0.6 fringe/pixel, when the



**Fig. 3.11** Comparison of fringe order variation along the  $y$ -axis with disk center as the origin by various methods.



**Fig. 3.12** Variation of total fringe along  $y$ -axis for top magnified tile.

magnification of the tile over the original image is 5.3. Figure 3.12 shows the variation of total fringe order along a vertical line passing through the load application point for top tile. It can be noted from the figure that in the optically magnified image the fringe order resolvable is up to 13 and the corresponding fringe gradient is 0.11 fringe/pixel. Thus OET has improved fringe order extraction in the stress concentration zones.

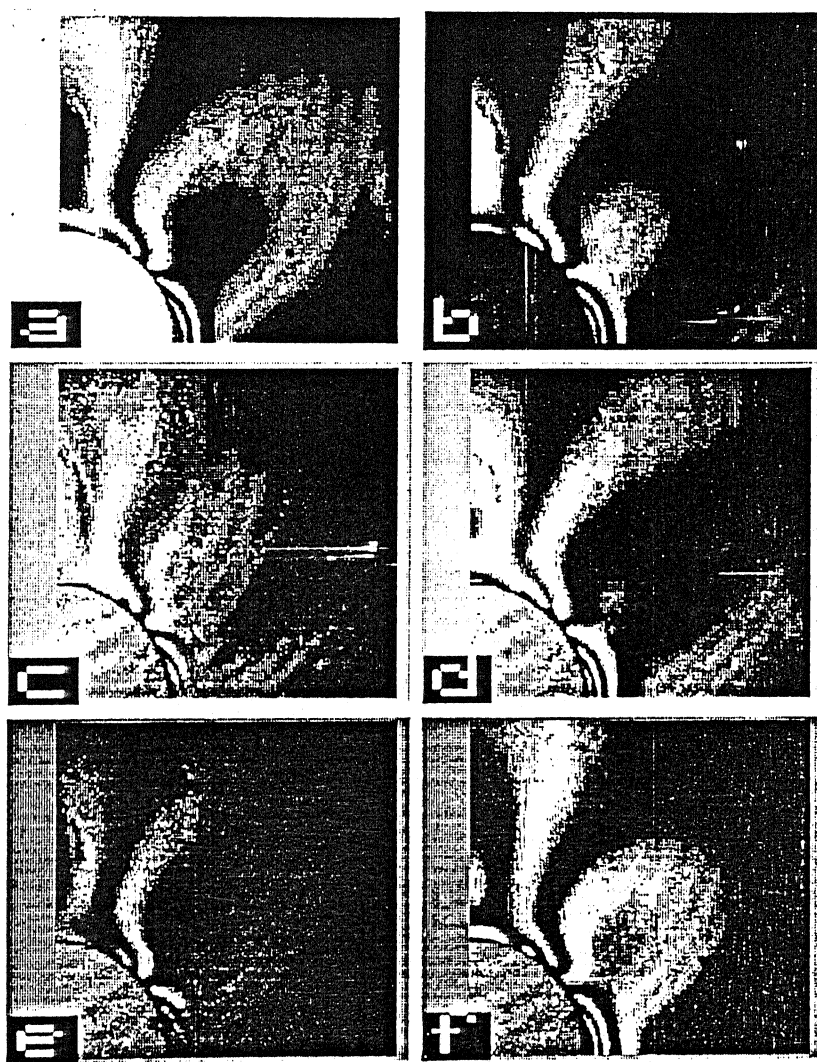


**Fig. 3.13** The sequence of six images those are recorded for phase shifting of magnified tile.

### 3.6 Application Of OET To A Plate With A Hole Under Uni-axial Tension

The stress concentration zone in a plate with a hole occurs at boundary of the horizontal diameter of the hole. To capture the images, CCD camera is equipped with a zoom lens and a 10 mm extender. Six images as per Table 2.1 are captured for this stress concentration zone. Figure 3.13 shows the captured magnified images. Using the procedure mentioned in Section 2.2, the phase map of this stress concentration zone is obtained. The phase map of the magnified tile is shown in Fig. 3.14(b).

The magnification of the overall image is 0.35 pixels/mm and for the magnified tile it is 0.12 pixels/mm. The magnification of the magnified tile over the original image ( $m/m_o$ ) is 2.92. The center of the hole of the plate is taken as the reference points for both the original image and the magnified tile to cement the tile. The phase of the magnified tile is unwrapped by using the unwrapping technique discussed in Section 2.4. Figure 3.15(a) shows the variation of total fringe order for the original image of plate with hole

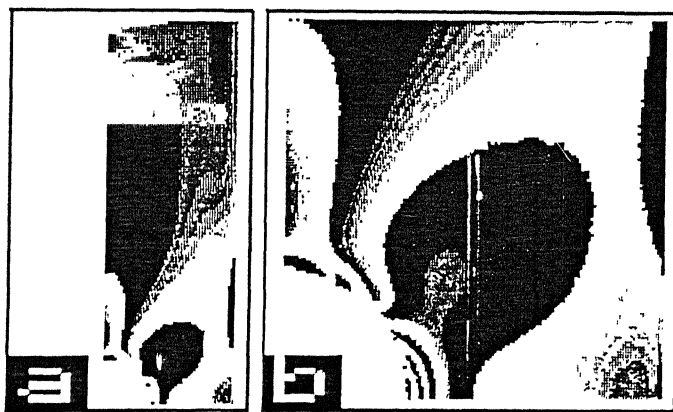
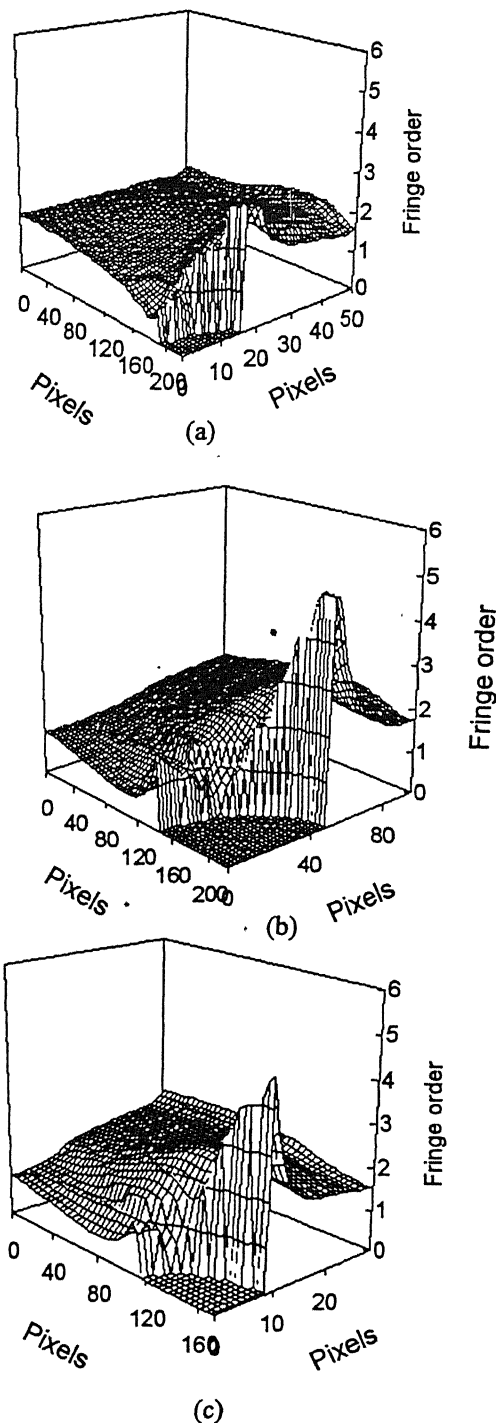


Fig. 3.14 Phase map. (a) One quarter of plate with a hole. (b) Magnified tile.



**Fig. 3.15** Three dimensional representation of unwrapped phase for the problem of plate with a hole. (a) Direct evaluation. (b) Magnified tile. (c) by OET

which is subjected to uni- axial tension. Figure 3.15(b) shows the variation of the total fringe order for the magnified tile. Figure 3.15(c) shows the variation of the total fringe order for the composite image of plate with a hole.

### 3.6.1 Performance Of The OET For Plate With A Hole Under Uni-axial Tension

To compare the performance one has to evaluate the theoretical fringe orders. To calculate the theoretical fringe orders at a point of the plate with a hole, the material stress fringe value  $F_\sigma$  is to be known. It is difficult to find directly the material stress fringe

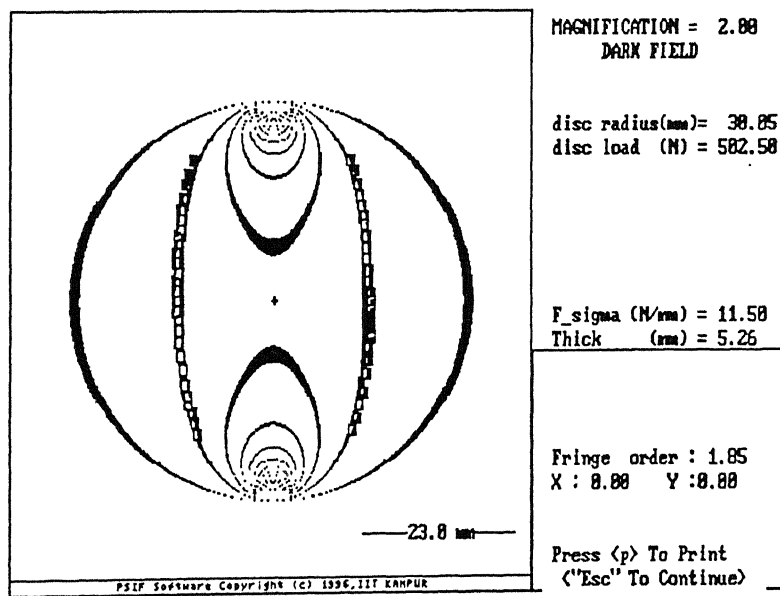
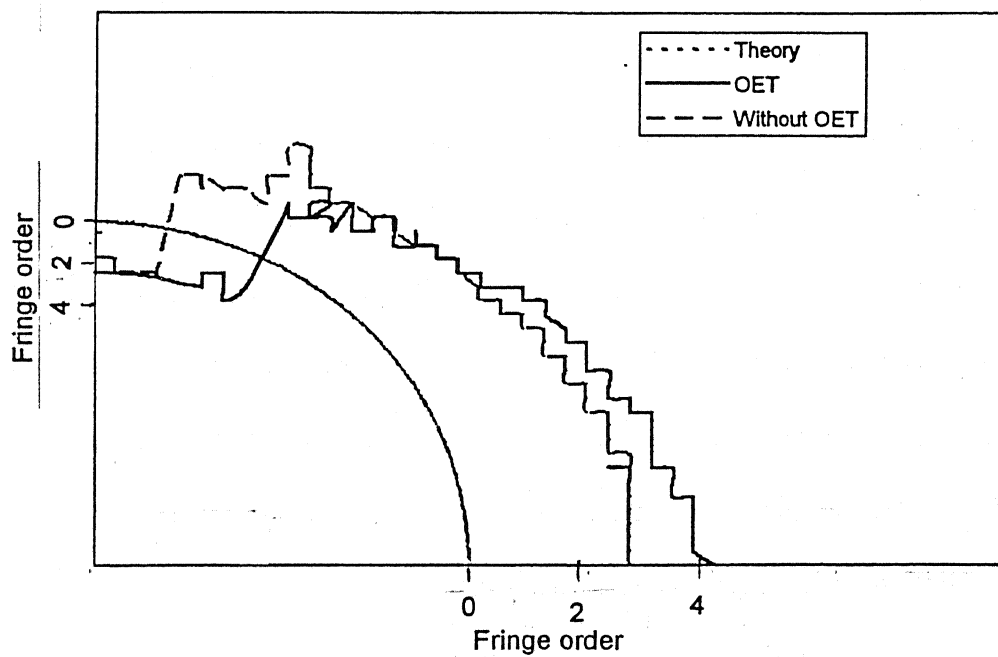


Fig. 3.16 The theoretically reconstructed fringe pattern of disk under diametral compression for the problem of plate with a hole.

value for plate with a hole specimen. The value of  $F_\sigma$  depends on the preparation method and age of the specimen. Circular disk under diametral compression specimen is used to find the  $F_\sigma$ . A circular disk is prepared from the same sheet of material, which is used to prepare the plate with a hole specimen. A circular disk of diameter 60.1 mm, thickness of 5.26 mm, and which is subjected to an diametral load of 502.6 N is analyzed. The  $F_\sigma$  of the circular disk under diametral compression is calculated using the least square method for 52 data points collected on the fringe areas. The  $F_\sigma$  value is found to be 11.5 N/mm/fringe. The accuracy of this value is verified by reconstructing the fringe pattern and comparing it with original fringe pattern. The reconstructed fringe pattern is shown in Fig. 3.16. Hence the  $F_\sigma$  value of plate with a hole is 11.5 N/mm/fringe.



**Fig. 3.17** Comparison of fringe order variation between OET and without OET along the inner boundary of the plate with a hole.

A plate with a finite hole is a finite geometry problem, theoretical solutions can be obtained from FEM. As the FEM solution for this problem is not readily available, the evaluation of total fringe order for a plate with a hole is not compared with theory. From the Fig. 3.17 it can be observed that by direct evaluation, the evaluation of total fringe order is limited to a value of 2.7 and by the OET, it is up to 4.3 at the inner diameter. Thus OET has improved fringe order extraction in the stress concentration zone.

### 3.7 Problem of OET For Ring Under Diametral Compression

The fringe field in the case of a ring under diametral compression is much more complex than that of the circular disk and the plate with a hole. The stress concentration zones in ring under diametral compression are at the load application points and along the inner boundary. Let us denote the stress concentration zone along the inner boundary as zone1 and the stress concentration zone at the load application point as zone2. To capture the magnified images for zone1, the CCD camera equipped with a zoom lens and a 10 mm extender is used and to capture the magnified images. For zone2, the CCD camera is equipped with a macro lens. Six images as per Table 2.1 are captured for this stress concentration zone. Figures 3.18(a) and 3.18(b) show the captured magnified images for zone1 and zone2 respectively. Using the procedure mentioned in Section 2.2, the phase maps of these stress concentration zones are obtained. Figure 3.19(b) and 3.19(c), show the phase maps for the optically magnified stress concentration along the inner boundary and at the load application point respectively.

The magnification of the overall image is 0.29 pixels/mm. The magnified tile1 is 0.14 pixels/mm. The magnification of the magnified tile1 over the original image ( $m_1/m_o$ )

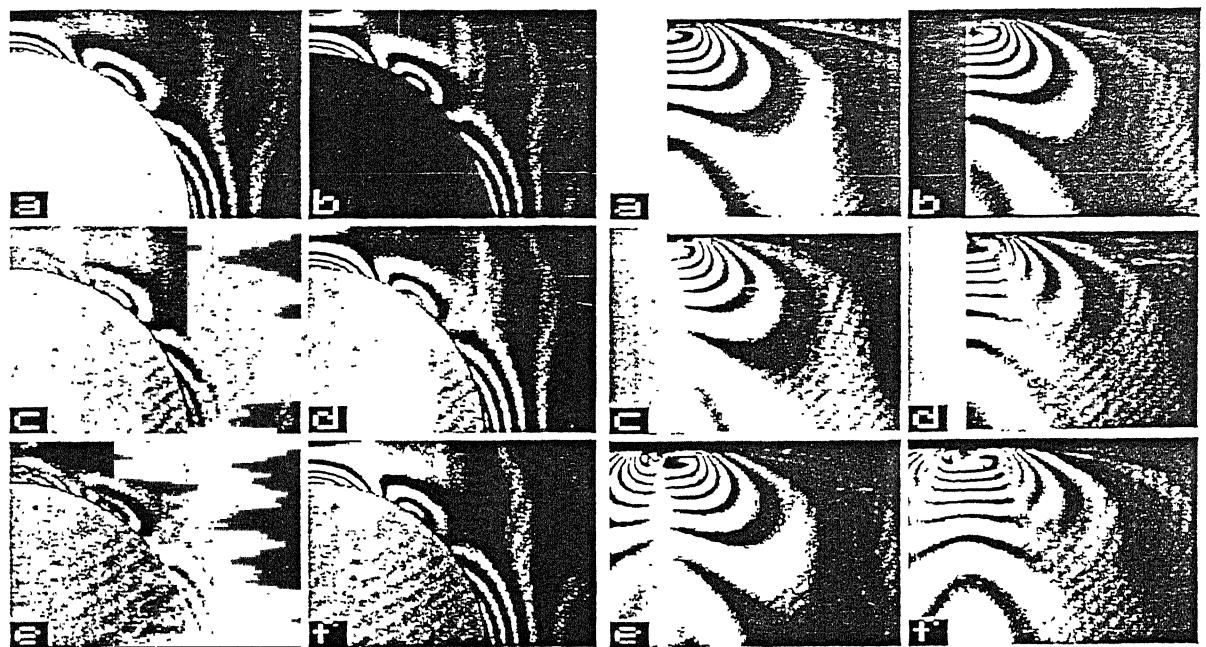


**Fig. 3.18** The sequence of six images those are recorded for phase shifting of tiles for the problem of ring under diametral compression.

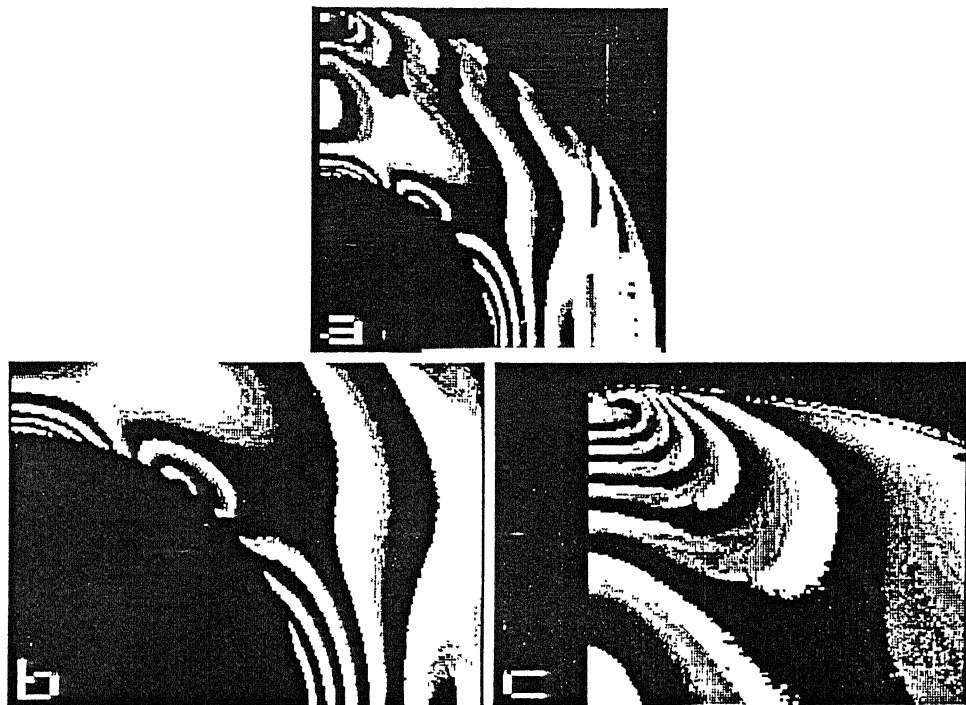


**Fig. 3.19** Phase map. (a) Ring as a whole. (b) Zone1 (c) Zone 2.

is 1.74. The center of the ring is taken as the reference points for both the original image and magnified tile1 to cement the tile. The phase of the magnified tile is unwrapped by using the unwrapping technique discussed in Section 2.4. Figure 3.20(b) shows the variation of the total fringe order for the magnified tile1. The magnification of the magnified tile2 is 0.625 pixels/mm. The magnification of the magnified tile2 over the original image ( $m_2/m_o$ ) is 3.8. The load application point of the ring is taken as the reference points for both the original image and magnified tile2 to cement the tile. The

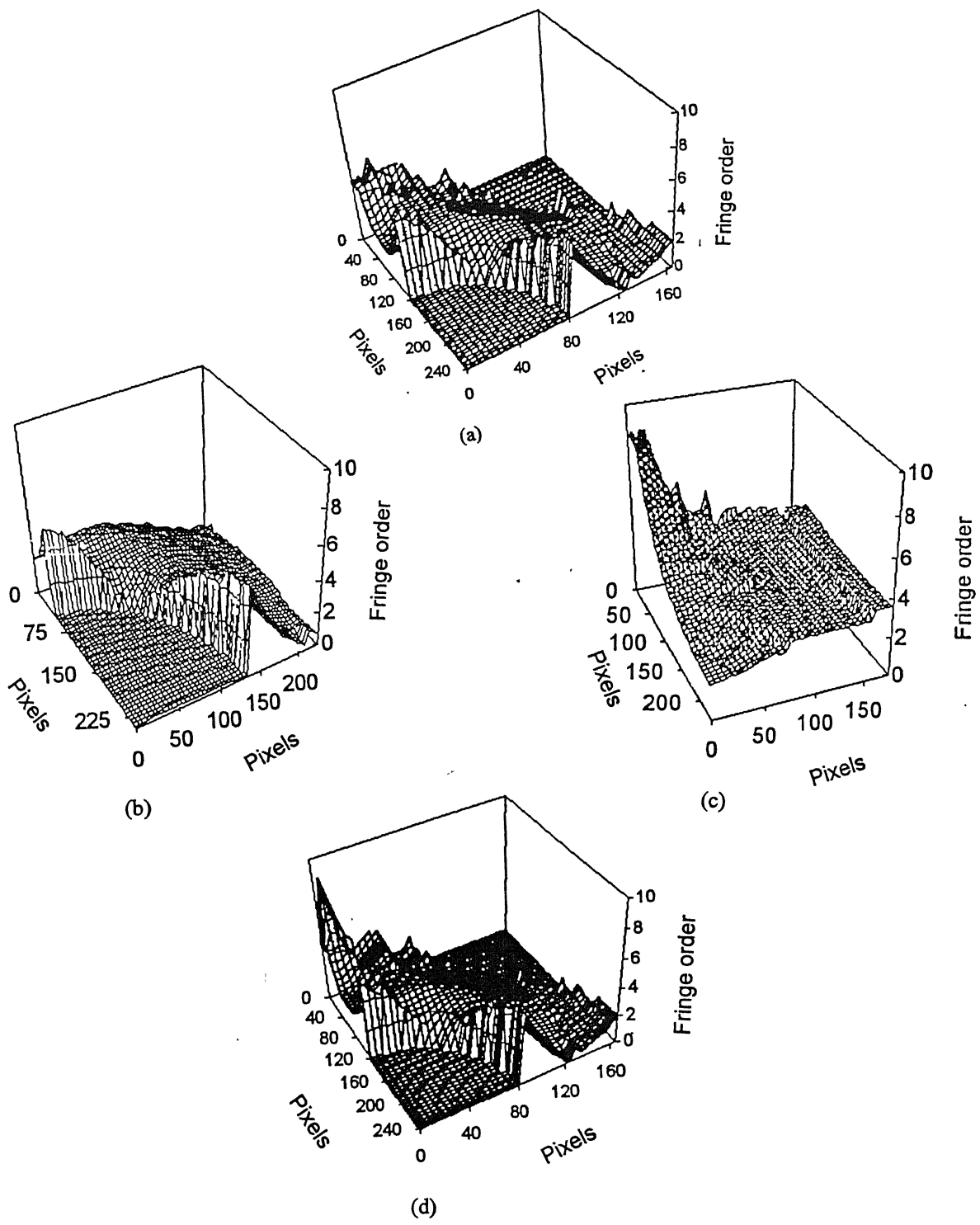


**Fig. 3.20** Three dimensional representation of unwrapped phase for the problem of ring under diametral compression. (a) Direct evaluation. (b) Zone1. (c) Zone2. (d) by OET.

phase of the magnified tile is unwrapped by using the unwrapping technique discussed in Section 2.4. Figure 3.20(c) shows the variation of the total fringe order for the magnified tile2. Figure 3.20(d) shows the variation of the total fringe order for the composite image.

### 3.7.1 Performance Of The OET For Ring Under Diametral Compression

To calculate the theoretical fringe orders at a point for the ring under diametral compression, the material stress fringe value  $F_\sigma$  is to be known. It is difficult to find directly the material stress fringe value for ring under diametral compression. Because an old specimen is used for the analysis, circular disk made from the same sheet was not available. The value of  $F_\sigma$  is found out by using the method of reconstruction. In this

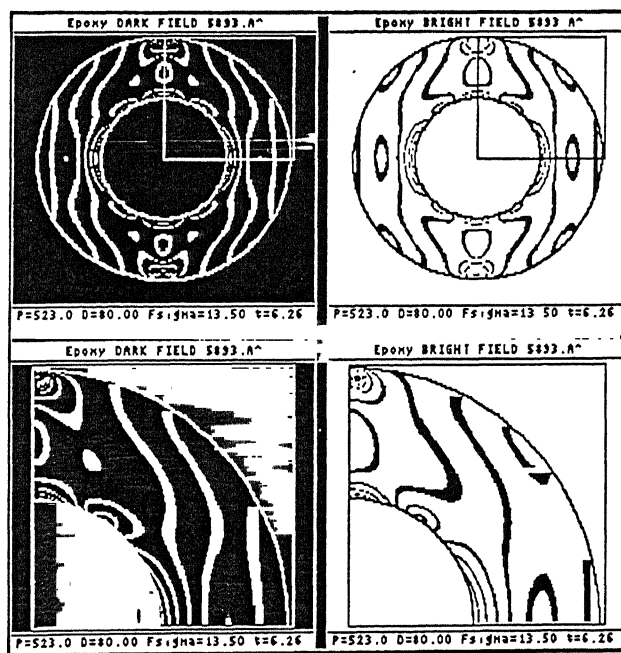


**Fig. 3.21** The theoretically reconstructed fringe pattern of ring under diametral compression.

method theoretical fringes are reconstructed in the dark field using the dimensions of the ring of loading conditions (Section 2.8.2) and an arbitrary value  $F_\sigma$ . This method is repeated until the reconstructed dark field matches with the dark field of captured image. The theoretical fringe are reconstructed using PHOTOSOFT\_H<sup>9</sup> software. The reconstructed fringes with material stress fringe value of 13.5 N/mm/fringe is shown in Fig. 3.21.

Figure 3.22 compares the variation of total fringe order along the inner boundary obtained directly and after OET with theory (Appendix-II). From the figure it is clear that by direct evaluation, the total fringe order is limited to a value of 3.9 along the horizontal

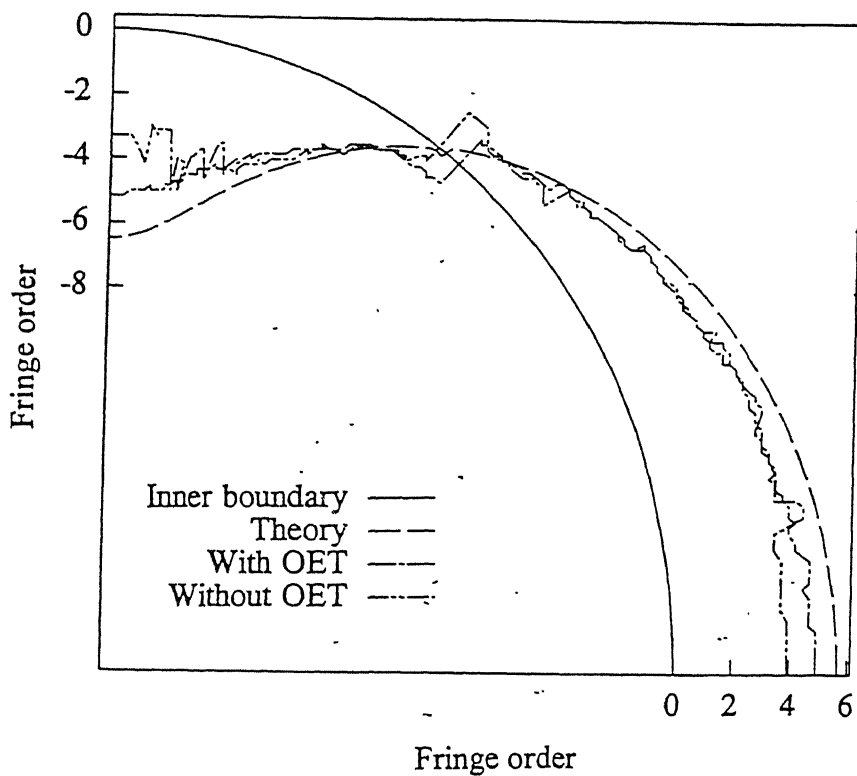


**Fig. 3.22** Comparison of fringe order variation along inner boundary of the ring by various methods.

inner diameter. With the OET, the fringe order resolvable is up to 5.0 along inner diameter. The fringe orders resolvable are 3.2 and 6.7 along the vertical diameter without OET and with OET respectively. The variation of total fringe order is also smoother with OET. Thus OET has improved fringe order extraction in the stress concentration zones.

### **3.8 Closure**

A new approach to image enhancement in high fringe gradient zones is presented and a systematic approach to cement the tiles to overall image is also discussed. The procedure is verified by estimating total fringe order variation for circular disk under diametral compression, plate with a hole under uni-axial tension and ring under diametral compression. It has been shown that OET has improved fringe order extraction in the stress concentration zones.

## **Chapter 4**

# **CONCLUSIONS AND SUGGESTIONS FOR FUTURE WORK**

### **4.1 Conclusions**

This thesis is a step towards complete automation of photoelastic analysis. Complete automation of photoelastic analysis requires both collection and its analysis to be automated. In this thesis, automation of data collection is implemented using phase shifting algorithms.

Evaluation of fractional retardation by phase shifting and its limitations are discussed in the thesis. Evaluation of total fringe order by phase unwrapping is discussed in detail. As detection of boundary and noise removal are important for the evaluation of total fringe order, they are also discussed in this thesis. As normal unwrapping algorithm fails for certain class of problem, a technique called unwrapping by tiling is implemented. The procedure is verified by estimating the total fringe order variation for a circular disk under diametral compression, a plate with a hole and a ring under diametral compression.

As intensity information is lost in high fringe density areas, the extraction of more fringe orders at the stress concentration by a new technique called Optical Enhanced Tiling (OET) is developed. A new approach to image enhancement in high fringe gradient zones is presented and a systematic approach to cement the tiles to the overall image is

also discussed. The procedure is verified by estimating total fringe order variation for a circular disk under diametral compression, a plate with a hole under uni-axial tension and a ring under diametral compression. It has been shown that OET has improved fringe order extraction in the stress concentration zone.

## **4.2 Suggestions For Future Work**

It is discussed that Patterson and Wang's algorithm for phase shifting fails to give complete phase retardation over the whole domain. Quiroga and Gonzales<sup>10</sup> have come up with new phase shifting algorithm recently. This algorithm can be implemented in future to get the unambiguous phase map to find the total fringe order for the whole domain.

In this thesis for phase unwrapping row seeding and column-wise scanning, and column seeding and row-wise scanning have been implemented. This algorithm fails when the shape of the body is complex like a multiply connected body. In the literature, investigators<sup>11-13</sup> have come up with random phase unwrapping. This can also be implemented in future.

To unwrap the phase of the phase map, boundary of the object has to be detected. In this thesis a simple boundary detection algorithm is discussed. This boundary detection algorithm fails when there is more than two boundary pixels in along the scanning direction. This algorithm can be extended to detect the boundary for complex shaped bodies.

# APPENDIX-I

This appendix describes the analysis of stress in a circular disk. The problem can be treated as superposition of Boussinique's and Lame's problems.

The stresses at any point in a circular disk under diametral compression is given by,

$$\sigma_{xx} = -\frac{2P}{\pi t} \left[ \frac{(R-y)x^2}{r_1^4} + \frac{(R+y)x^2}{r_2^4} - \frac{1}{d} \right]$$

$$\sigma_{yy} = -\frac{2P}{\pi t} \left[ \frac{(R-y)x^2}{r_1^4} + \frac{(R+y)^3}{r_2^4} - \frac{1}{d} \right]$$

$$\tau_{xy} = \frac{2P}{\pi t} \left[ \frac{(R-y)^2 x}{r_1^4} - \frac{(R+y)^2 x}{r_2^4} \right]$$

and

$$r_1^2 = x^2 + (R-y)^2$$

$$r_2^2 = x^2 + (R+y)^2$$

Where,  $P$  is the load applied.

$R$  is the disk radius.

$d$  is the disk diameter.

$t$  is the thickness of disk.

## APPENDIX-II

In two dimensional, the distribution of stresses in a circular ring under diametral compression [Fig. A2.1(a)] can be represented as combination of the problem of disk under diametral compression [Fig. A2.1(b)] and a ring [Fig. A2.1(c)].

If the normal and the tangential tensions acting on the inner rim of the ring [Fig. A2.1(c)] as equal and opposite to the tensions acting on the cylindrical surface of the radius  $r$  in a disk [Fig. A2.1(a)], the stress-distribution in the case of Fig. A2.1(a) will be obtained by summing the stresses corresponding to Figs. A2.1(b) and A2.1(c).

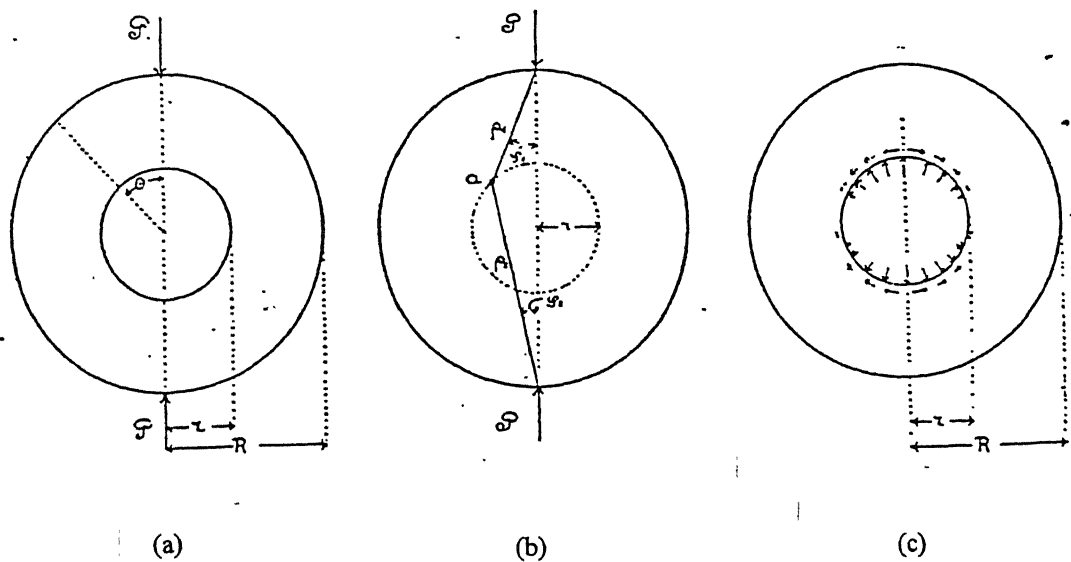


**Fig. A2.1** Distribution of stresses in a circular ring under diametral compression.

(a) Ring. (b) Circular disk. (c) Ring.

Stress at any point for the ring (Fig. A2.3) is given by,

$$\sigma_{rr} = \frac{2P}{\pi R} \left[ 0.506 \frac{r^2}{\rho^2} \frac{R^2 - \rho^2}{R^2 - r^2} + \left( -2.268 - 0.4832 \frac{R^4}{\rho^4} + 2.752 \frac{R^2}{\rho^2} \right) \cos 2\theta \right.$$

$$+ \left( -0.3691 \frac{\rho^2}{R^2} + 0.2261 \frac{\rho^4}{R^4} - 0.0368 \frac{R^6}{\rho^6} + 0.1798 \frac{R^4}{\rho^4} \right) \cos 4\theta$$

$$+ \left( -0.06504 \frac{\rho^4}{R^4} + 0.05013 \frac{\rho^6}{R^6} - 0.0041319 \frac{R^8}{\rho^8} + 0.01904 \frac{R^6}{\rho^6} \right) \cos 6\theta$$

$$+ \left( -0.008758 \frac{\rho^6}{R^6} + 0.007352 \frac{\rho^8}{R^8} - 0.00040795 \frac{R^{10}}{\rho^{10}} + 0.0018146 \frac{R^8}{\rho^8} \right) \cos 8\theta$$

$$+ \left( -0.000788 \frac{\rho^8}{R^8} + 0.0006911 \frac{\rho^{10}}{R^{10}} - 0.0000296 \frac{R^{12}}{\rho^{12}} + 0.001054 \frac{R^{10}}{\rho^{10}} \right)$$
  

$$\sigma_{\theta\theta} = \frac{2P}{\pi R} \left[ -0.506 \frac{r^2}{\rho^2} \frac{R^2 + \rho^2}{R^2 - r^2} + \left( 2.268 - 6.324 \frac{\rho^2}{R^2} + 0.4832 \frac{R^4}{\rho^4} \right) \cos 2\theta \right.$$

$$+ \left( 0.3691 \frac{\rho^2}{R^2} - 0.6783 \frac{\rho^4}{R^4} + 0.0368 \frac{R^6}{\rho^6} - 0.0599 \frac{R^4}{\rho^4} \right) \cos 4\theta$$

$$+ \left( 0.06504 \frac{\rho^4}{R^4} - 0.10026 \frac{\rho^6}{R^6} + 0.0041319 \frac{R^8}{\rho^8} - 0.00952 \frac{R^6}{\rho^6} \right) \cos 6\theta$$

$$+ \left( 0.008758 \frac{\rho^6}{R^6} - 0.01225 \frac{\rho^8}{R^8} + 0.00040795 \frac{R^{10}}{\rho^{10}} - 0.0010888 \frac{R^8}{\rho^8} \right) \cos 8\theta$$

$$+ \left( 0.000788 \frac{\rho^8}{R^8} - 0.001037 \frac{\rho^{10}}{R^{10}} + 0.0000296 \frac{R^{12}}{\rho^{12}} - 0.00008475 \frac{R^{10}}{\rho^{10}} \right) \cos 10\theta ]$$

$$\begin{aligned}
\tau_{r\theta} = & \frac{2P}{\pi R} \left[ \left( 2.268 - 3.162 \frac{\rho^2}{R^2} - 0.4832 \frac{R^4}{\rho^4} + 1.376 \frac{\rho^2}{R^2} \right) \sin 2\theta \right. \\
& + \left( 0.3691 \frac{\rho^2}{R^2} - 0.4522 \frac{\rho^4}{R^4} - 0.0368 \frac{R^6}{\rho^6} + 0.1198 \frac{R^4}{\rho^4} \right) \sin 4\theta \\
& + \left( 0.06504 \frac{\rho^4}{R^4} - 0.0752 \frac{\rho^6}{R^6} - 0.0041319 \frac{R^8}{\rho^8} + 0.01428 \frac{R^6}{\rho^6} \right) \sin 6\theta \\
& + \left( 0.008758 \frac{\rho^6}{R^6} - 0.009802 \frac{\rho^8}{R^8} - 0.00040795 \frac{R^{10}}{\rho^{10}} + 0.0014517 \frac{R^8}{\rho^8} \right) \sin 8\theta \\
& \left. + \left( 0.000788 \frac{\rho^8}{R^8} - 0.0008638 \frac{\rho^{10}}{R^{10}} - 0.0000296 \frac{R^{12}}{\rho^{12}} + 0.0001054 \frac{R^{10}}{\rho^{10}} \right) \sin 10\theta \right]
\end{aligned}$$

Finding the stress at any point on the circular disk under diametral compression is explained in Appendix-I.

## REFERENCES

1. K. Ramesh and S. K. Mangal, "Data Acquisition Techniques in Digital Photoelasticity : A review," *Opt. And Lasers In Eng.*, (in press).
2. A. Asundi, "Phase shifting in photoelasticity", *Expl. Techniques*, 17, 19-23 (1993).
3. F. W. Hecker and B. Morche, "Computer-aided measurement of relative retardations in plane photoelasticity", *Experimental Stress Analysis*, (ed) H. Wieringa, Martinus Nijhoff Publishers, Dordrecht, The Netherlands, 535-542 (1986).
4. E. A. Patterson and Z. F. Wang, "Towards full-field automated photoelastic analysis of complex components", *Strain*, 27, 49-56 (1991).
5. A. V. S. S. S. R. Sarma, S. A. Pillai, G. Subramanian, T. K. Varadan, "Computerized image processing for whole-field determination of isoclinics and isochromatics", *Expl. Mechanics*, 32, 24-39 (1992).
6. K. Ramesh and V. Ganapathy, "Phase-shifting methodologies in photoelastic analysis-the application of Jones calculus", *J. Strain Analysis*, 31, 423-432 (1996).
7. M. M. Frocht, *Photoelasticity vol. I*, John Wiley & Sons Inc., London, 42 (1941).
8. V. Ganapathy, *Application of phase-shifting interferometric technique to automate photoelastic analysis*, M. Tech Thesis, I. I. T., Kanpur (1995).
9. K. Ramesh, "PHOTOSOFT\_H: A comprehensive photoelasticity simulation module to teach the technique of photoelasticity." *International Journal of Mechanical Engg Education*, 25(4) 306-324 (1997).

10. J. A. Quiroga and A. Gonazales-Cano, "Phase measuring extraction of isochromatics of photoelastic fringe patterns", *Appl. Opt.*, 36, 8397-8402 (1997).
11. K. A. Stetson, J. Wahid and P. Gauthier, "Noise-immune phase unwrapping by use of calculated wrap regions", *Appl. Opt.*, 36, 4830-4838 (1997).
12. J. A. Quiroga and E. Bernabeu, "Phase-unwrapping algorithm for noisy phase-map processing", *Appl. Opt.*, 33, 6725-6731 (1994).
13. K. A. Stetson, "Phase-step interferometry of irregular shapes by using an edge-following algorithm", *Appl. Opt.*, 31, 5320-5325 (1992).
14. A. Jain, *Fundamentals of Digital Image Processing*, Prentice-Hall (1989).
15. R. C. Gonzalez and R. E. Woods, *Digital Image Processing*, Addison-Wesley Publishing Company (1992).
16. S. Timoshenko, "On the distribution of stresses in a circular ring compressed by two forces acting along a diameter", *Phil. Mag.*, 44, 1014-1019 (1922).
17. L. S. Srinath, M. R. Raghavan, K. Lingaiah, G. Gargesha, B. Pant and K. Ramachandra, *Experimental Stress Analysis*, Tata McGraw-Hill (1984).
18. K. Ramesh and K. Muralidhar, *Short Term Course On Computer Applications In Experimental Mechanics*, Quality improvement program, I. I. T., Kanpur (1991).